Karst hydrological changes during the Late-Holocene in Southwestern China

Chao-Jun Chen [a, b, c, 1], Ran Huang [a, b, c, 1], Dao-Xian Yuan [a, c], Jian Zhang [a, d], Hai Cheng [e], You-Feng Ning [e], Tsai-Luen Yu [f, g], Chuan-Chou Shen [f, g, h], R. Lawrence Edwards [i], Xiao-Yong Long [a], Tao Wang [a], Si-Ya Xiao [a, c], Yao Wu [a, c], Zi-Qi Liu [j], Ting-Yong Li [b, *], Jun-Yun Li [a, c, **]

[a] Chongqing Key Laboratory of Karst Environment, School of Geographical Sciences, Southwest University, Chongqing, 400715, China
[b] Yunnan Key Laboratory of Plateau Geographical Processes & Environmental Changes, Faculty of Geography, Yunnan Normal University, Kunming, 650500, China
[c] Key Laboratory of Karst Dynamics, MNR & Guangxi, Institute of Karst Geology, CAGS, Guilin, 541004, China
[d] Environnements et Paléoenvironnements Océaniques et Continentaux (EPOC), UMR CNRS, 5805, Université de Bordeaux, Pessac, France
[e] Institute of Global Environmental Change, Xi'an Jiaotong University, Xi'an, 710049, China
[f] High-precision Mass Spectrometry and Environment Change Laboratory (HISPEC), Department of Geosciences, National Taiwan University, Taipei, 10617, Taiwan
[g] Research Center for Future Earth, National Taiwan University, Taipei, 10617, Taiwan
[h] Global Change Research Center, National Taiwan University, Taipei, 10617, Taiwan
[i] Department of Earth Sciences, University of Minnesota, Minneapolis, MN, USA
[j] School of Karst Science, Guizhou Normal University, Guiyang, 550001, China

ARTICLE INFO

ABSTRACT

The frequent alternation between droughts and floods in the karst regions of Southwestern China has a serious impact on the ecological environment and socio-economic development. Although some high-resolution records for this region have been published, there is a lack of multi-proxy geological records that could be used to reconstruct the relationships between the changes in the Asian summer monsoon (ASM) and the regional hydrology and ecological environment since the Late Holocene. In this study, the history of the ASM from 3109 to 694 yr BP with a mean temporal resolution of 2.5 yr is reconstructed based on 47 high-precision ^{230}Th dating results (mean 2-sigma error of ± 14 yr), 959 pairs of δ^{18}O/δ^{13}C data, and multiple trace element analyses of a stalagmite from Shijiangjun (SJJ) Cave in the karst area of Southwestern China. The positive δ^{18}O and δ^{13}C excursions accurately recorded eight interdecadal-centennial weak summer monsoon events at ~779, 1013−911, 1282−1172, 1736−1638, 1961−1864, 2472−2375, 2931−2818, and 3050−3014 yr BP. The cross-wavelet spectrum analysis of the δ^{18}O and δ^{13}C of stalagmite SJJ7 indicates that they have similar periods. The 7 yr period of the δ^{18}O record was determined to have the maximum contribution rate (36.8%) to the periods using ensemble empirical mode decomposition (EEMD) analysis. In the Late Holocene, the weak ASM events were dominated by the southward shift of the Intertropical Convergence Zone (ITCZ) and the frequent El Niño events on an interdecadal-centennial timescale. The southward migration of the ITCZ lead to frequent El Niño events, and the resultant Hadley Circulation and Walker Circulation were weakened, leading to a weak ASM and changes in the hydrological conditions in the monsoon region. The δ^{13}C values of the stalagmite changed relatively slowly compared with the δ^{18}O values, which may indicate that the degradation and restoration of the regional ecological environment caused by abrupt changes in the climate is a relatively slow process. When the summer monsoon decreased, the stalagmite's Mg/Ca and Sr/Ca ratios were relatively high due to CO_2 degassing, and the prior calcite precipitation (PCP)/prior aragonite precipitation (PAP) increased in the karst zone. However, the Mg/Ca ratio increased and the Sr/Ca ratio rapidly decreased during the calcite deposition due to differences in the crystal structures and partition coefficients of

---

* Corresponding author.
** Corresponding author. Chongqing Key Laboratory of Karst Environment, School of Geographical Sciences, Southwest University, Chongqing, 400715, China.
  E-mail addresses: cdlity@163.com (T.-Y. Li), jxljy@swu.edu.cn (J.-Y. Li).
[1] Joint first authors: Chao-Jun Chen and Ran Huang.

aragonite and calcite. The dark layers in stalagmite SJJ7 correspond to transition from heavy to light δ^{18}O values, reflecting the transition in the ASM. The pulsed increases in the elements (Mn, Fe, Al, and Si) in the dark layers reflect the stronger mechanical transport caused by more rainfall. The multi-proxy analysis of this stalagmite may reflect the interactions between the changes in the ASM and the atmosphere-hydrosphere-pedosphere-biosphere-lithosphere in the karst critical zone during the Late Holocene.

1. Introduction

The ecological environment is fragile in the karst regions of Southwestern China. This area is deeply influenced by the Asian summer monsoon (ASM) and is extremely sensitive to global climate change. In addition, there is a prominent contradiction between the anthropogenic activities and the environment, which has caused a series of serious severe ecological and socio-economic problems (Yuan, 2015; Zeng et al., 2016). The historical data from 1900 to 2012 AD indicated that drought and flood disasters have frequently occurred in the karst areas of Southwestern China, especially in Guizhou Province (Guo et al., 2015). However, the limited meteorological data available for this region limits our understanding of climate change on interdecadal or even longer time scales. Therefore, paleoclimate records preserved in geological archives are crucial to resolving this issue and assessing the impact of future climate change on the ecological environment.

On the orbital time scale, an external driving force (solar radiation) dominates the variation in the ASM (Wang et al., 2017). However, the internal feedbacks (El Niño-Southern Oscillation, Atlantic meridional overturning circulation, and the Intertropical Convergence Zone) of the climate system are usually responsible for the changes in the ASM on short time scales (Wan et al., 2011; Wang et al., 2017; Cheng et al., 2019). As a key stage in the connection between the present and past, the Late Holocene may have contained a series of abrupt centennial-millennium climate events (Wang et al., 2005; Cook et al., 2010; Conroy et al., 2017; Kathayat et al., 2017; Tan et al., 2018). However, the evolution of the ASM is still unclear on the interdecadal-centennial scale (Tan et al., 2016). Pollen from lake sediments indicates that the temperature and humidity in Southwestern China gradually decreased during the Late Holocene (Xiao et al., 2014). Interdecadal-centennial scale changes in the ASM may have led to spatial differences in the changes in the regional hydrological and ecological environment (Xiao et al., 2014; Conroy et al., 2017). However, it is difficult to accurately reconstruct these regional hydrological changes because of the large errors involved in lake sediment dating and the low resolution of the samples. In addition, tree-ring paleoclimate records are very sparse in Southwestern China (Duan et al., 2014; Wang et al., 2005). The existing high-resolution summer monsoon reconstruction for this area is mostly based on a single indicator, i.e., stalagmite δ^{18}O (Duan et al., 2014; Wang et al., 2005), and the significance of the hydrological and climatological indicators of stalagmite δ^{18}O on the annual-interdecadal scale is controversial (Tan et al., 2016). Therefore, it is necessary that multiple stalagmite proxies be used to synthetically reconstruct the paleoclimate and paleoenvironment (Cheng et al., 2019).

Stalagmites contain many substitute proxies for paleoclimate and paleoenvironment, such as δ^{18}O, δ^{13}C, Mg/Ca, Sr/Ca, growth rate, gray scale, U concentration, and ^{87}Sr/^{86}Sr (Baldini et al., 2012; Fairchild et al., 2006; Fairchild and Treble, 2009; Johnson et al., 2006). X-ray fluorescence is a fast and reliable technique for analyzing trace element compositions of stalagmites (Borsato et al., 2007; Vansteenberge et al., 2019; Li et al., 2019). The trace elements

and magnetic minerals can reflect regional hydrological changes and can be used to reconstruct past extreme drought and flood events (Cruz et al., 2007; Fairchild and Treble, 2009; Zhu et al., 2017; Zhang et al., 2018). The trace element concentrations are related to the water dissolved and undissolved chemical phases (Baldini et al., 2012; Hartland et al., 2011, 2012). The particle and colloid elements (e.g., Mn, Fe, Al, and Si) play an important role in the reconstruction of extreme climate events and paleoenvironment changes (Belli et al., 2017; Vansteenberge et al., 2019; Dill, 2020). The peak Fe and Al contents correspond to the flood horizon, and thus they reflect drought and flood events (Dasgupta et al., 2010). The variations in the Si/Ca ratios and Mn and Fe contents can also record changes in the regional hydrology (Dill, 2020; Hu et al., 2005). Mn, Fe, Al, and Si are generally adsorbed by clay minerals (kaolinium, montmorillonite, chlorite, and illite) in the soil and soil organic matter, and they are transported by the colloids and particles in the drip water (Wassenburg et al., 2012; Belli et al., 2017; Dill, 2020). However, Ca, Mg, Ba, and Sr are usually transported into the stalagmite in the dissolved phase in the drip water (Wassenburg et al., 2012; Belli et al., 2017). The crystal structures of clay minerals differ in different climatic environments (Dill, 2020). Yang et al. (Yang et al., 2011) reported that the proportion of clay minerals (kaolinium, montmorillonite, and illite) in soil changes as the karst rocky desertification in Southwest China transitions from mild to severe. These multiple proxies for stalagmite analysis have a great potential for reconstructing the changes in the regional hydrological environment. In addition, the karst area of Southwestern China, which supports a very fragile ecological environment, lacks high-resolution multi-proxy paleoclimate records controlled by high-precision chronology. The analysis of multiple stalagmite proxies can help us to reasonably interpret the meaning of these proxies and to more accurately reconstruct the evolution of the climate and regional ecological environment.

In summary, in this study, we investigated the following three issues: (1) How the evolution of the ASM in the Late Holocene affected the karst environment in Southwestern China on the interdecadal−centennial scale. (2) The relationship between the different stalagmite proxies and the change in the ASM. (3) What are the driving factors in the evolution of the ASM. We investigated these issues based on the analysis of stalagmite SJJ7 (maximum concentration of ^{238}U up to 47.5 ppm) from Shijiangjun (SJJ) cave, Guizhou Province, Southwestern China. We established an accurate age model for the Late Holocene based on high-precision ^{230}Th dating. In addition, we analyzed the δ^{18}O, δ^{13}C, Sr/Ca, Mg/Ca, Mn, Fe, Al, and Si data for the layers of stalagmite SJJ7 and reconstructed the evolution of the hydrological and ecological environment of this karst area during the Late Holocene. The results of this study are very important for predicting future climate change and for responding to extreme climate events. In addition, they are conducive to restoring rocky desertification and remediating the damage caused by socio-economic development.

2. Cave and geographic background

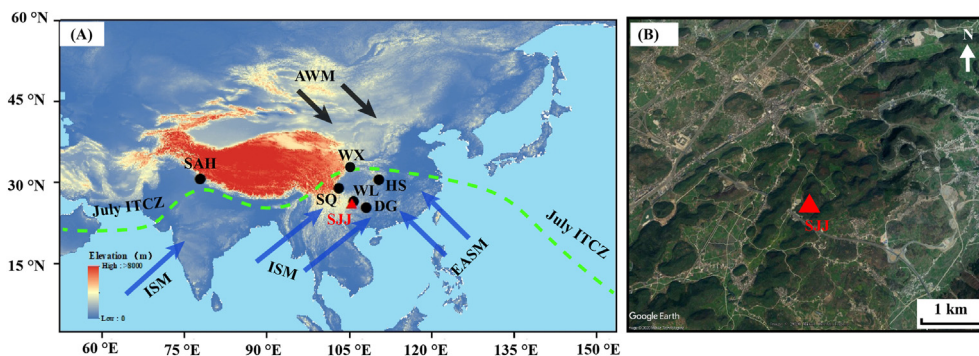Shijiangjun Cave (26.2°N, 105.5°E, 1300 m a.s.l.) is located in

Fig. 1. (A) Location of Shijiangjun Cave and other paleoclimate records. The red triangle indicates the location of Shijiangjun (SJJ) Cave (this study); the black dots indicate Dongge Cave (DG) (Duan et al., 2014), Shenqi Cave (SQ) (Tan et al., 2018), Wanxiang Cave (WX) (Zhang et al., 2008), Heshang Cave (HS) (Hu et al., 2008), Wulu cave (WL) (Zhao et al., 2020), and Sahiya Cave (SAH) (Kathayat et al., 2017). The blue arrows represent the surface wind directions of the ISM and the East Asian summer monsoon (EASM), the black arrows represent the surface wind direction of the Asian winter monsoon (AWM), and the green dotted line represents the ITCZ's position in July (Han et al., 2016). (B) Landforms around SJJ Cave (Picture came from Google Earth). The red triangle indicates the location of SJJ Cave. (For interpretation of the references to colour in this figure legend, the reader is referred to the Web version of this article.)

Qiyanqiao Town, Xixiu District, Anshun City, Guizhou Province, Southwestern China (Fig. 1). It is located in the gradual slope of the eastern part of the Yunnan-Guizhou Plateau. SJJ cave is developed in Middle and Upper Triassic, intermediate to thick limestone dolomite (Duan et al., 2015). The natural entrance of the cave is 2 m high and 1.5 m wide, and the entire length of the cave is about 500 m. The airflow and air exchange between the cave and the outside are very limited, and the temperature in the cave remains at ~15 °C throughout the year. There are abundant vertical fissures in the ceiling, stalagmites, and stalactites in the cave (Liu et al., 2008). The landform of the area in which the cave is located is a peak cluster depression (Fig. 1B). The top of the cave is covered by bedrock with a thickness of about 100 m, and shrub vegetation is developed. The thickness of the soil overlying the cave is less than 5 cm, and the ecological environment sensitively responds to changes in the regional hydrology (Duan et al., 2015). The changes in the trace element composition of the stalagmite are also influenced by soil erosion (Belli et al., 2017). When the vegetation coverage decreases, soil particles are more easily transported into the karst system (Belli et al., 2017).

The area in which SJJ cave is located is strongly affected by the ASM, and the water vapor in the local rainy season mainly comes from the Indian Ocean and the Pacific Ocean (Fig. 1A). The mean annual rainfall in Guiyang (26°58′N, 106°72′E, 1100 m a.s.l.), which is 70 km northeast of SJJ cave, was 1130 mm during 1951−2017 AD. The rainfall from May to August accounts for 80% of the annual rainfall. The observation data from Guiyang station from 1988 to 1992 revealed that the mean $\delta^{18}O$ value was −8.0‰ V-SMOW in summer (June to August), which was significantly more negative than that in winter (−4.3‰ V-SMOW) (December−February) (Fig. S1).

3. Samples and methods

3.1. X-ray diffraction analysis and scanning electron microscopy of stalagmite SJJ7

Stalagmite SJJ7 is cylindrical, with diameters of about 90 mm at the bottom and about 80 mm at the top (Fig. 2A). After longitudinal cutting and polishing along its growth axis, it was determined that its profile was characterized by the alternate distribution of yellow-brown (dark layers) and white layers, and its growth was continuous without any significant hiatuses in deposition. The total length of the stalagmite measured along its growth axis is 254 mm.

Using a dental drill with a diameter of 1 mm, 6 powder samples (60 mg each, A−F in Fig. S2) were drilled along the growth axis at 25 mm, 68 mm, 79 mm, 119 mm, 170 mm, and 220 mm. The X-ray diffractometer (XRD) (SMARTLAB 3) at the Institute of Frontier Science and Technology of Xi'an Jiaotong University was used for the analyses. The XRD spectra were obtained from 10° to 90° 2θ (Zhang et al., 2014a). The diffraction patterns of the samples were analyzed using the MDI jade 6.5 software (Song et al., 2013).

In the stalagmite profile, there are seven obvious yellow-brown dark layers (labeled as a−g, the thickness of 1.5−6 mm; Fig. 2A). The depths and ages of these dark layers are reported in Supplementary Table S1. A small slice (6 mm long, 5 mm wide, 2 mm thick; Fig. 2A) was taken from the fourth dark layer of the stalagmite and was coated with a conductive film (Zhang et al., 2014a). The scanning electron microscope (SEM) (SU35000102) at the State Key Laboratory of Silkworm Genome Biology of Southwest University was used to observe the fine structural differences between the light and dark layers.

3.2. U-Th dating

Forty-nine powder samples (10−50 mg) were collected parallel to the growth layers using a dental drill with a diameter of 1 mm from the polished profile of the stalagmite for U-Th age testing. The sampling locations are shown in Fig. 2A. The U and Th were separated using the standard chemical procedures described by Edwards et al. (1987), Shen et al. (2012), and Cheng et al. (2013). The ^{230}Th dating d was completed in the High-precision Mass Spectrometry and Environment Change Laboratory (HISPEC) of National Taiwan University (3/49) and the Isotope Laboratory of the Institute of Global Environmental Change of Xi'an Jiaotong University (46/49) using a multi-collector inductively coupled plasma mass spectrometer (MC-ICP-MS, Neptune-Plus). The uncertainties in the U−Th isotopic data were calculated offline at the 2σ level, including corrections for blanks, multiplier dark noise, abundance sensitivity, and contents of the same nuclides in the spike solution (Cheng et al., 2016). The decay constant used for ^{230}Th was $9.1705 \times 10^{-6} \ yr^{-1}$ (Cheng et al., 2013), that used for ^{234}U was $2.82206 \times 10^{-6} \ yr^{-1}$ (Cheng et al., 2013), and that used for ^{238}U was $1.55125 \times 10^{-10} \ yr^{-1}$ (Jaffey et al., 1971). An initial $^{230}Th/^{232}Th$ atomic ratio of $(4.4 \pm 2.2) \times 10^{-6}$ was assumed for the correction of the ^{230}Th ages. These are the values for materials in secular equilibrium with the bulk Earth $^{232}Th/^{238}U$ value.
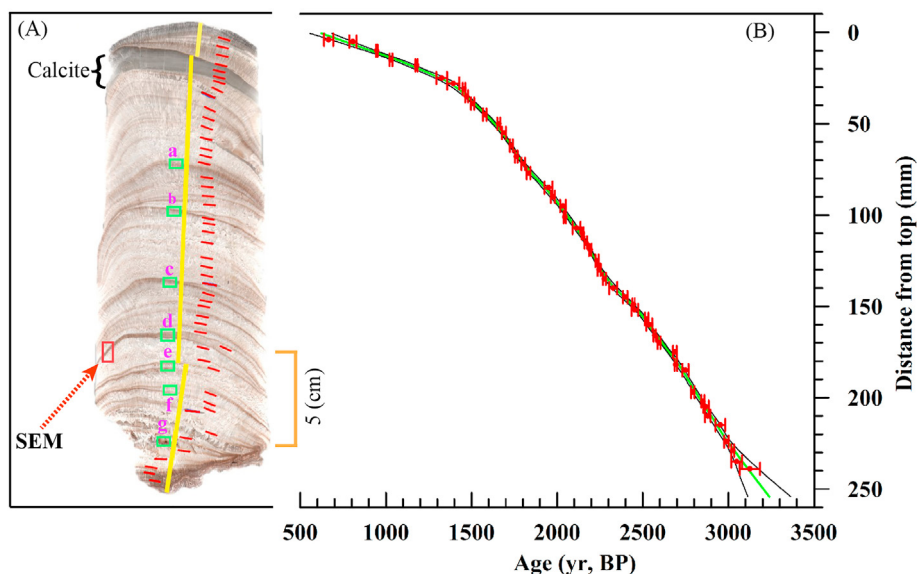
Fig. 2. (A) Profile of stalagmite SJJ7. The yellow vertical bars show the path of the stable isotope sampling and the trace element scanning. The short red lines show the location of the U−Th dating samples. The green boxes (a−g) indicate the horizons of the seven dark layers in the stalagmite's profile, and the small red box at the bottom left section shows the location of the SEM analysis. **(B) Chronological model of stalagmite SJJ7.** The green solid line is the chronological curve obtained using the Model Age software, the black solid line represents the 95% confidence band, and the red error bars represent the dating points and the error ranges. (For interpretation of the references to colour in this figure legend, the reader is referred to the Web version of this article.)

3.3. Carbon and oxygen stable isotope analyses

959 samples in total were collected for isotopic analysis using a dental drill with a diameter of 0.5 mm from the polished profile along the central growth axis of the stalagmite (Fig. 2A). Each sample was drilled at intervals of 0.25 mm. The $\delta^{18}O$ and $\delta^{13}C$ analyses of stalagmite SJJ7 were performed using the Delta V Plus isotope ratio mass spectrometer equipped with a Kiel IV Carbonate Device at the Geochemistry and Isotope Laboratory of Southwest University. One standard sample (SWU-1) was tested every seven samples. The results are reported relative to the Vienna-Pee Dee Belemnite (V-PDB) standard. The analytical error ($\pm1\sigma$) is less than 0.1‰ for $\delta^{18}O$ and less than 0.06‰ for $\delta^{13}C$ (Li et al., 2011).

3.4. Trace element analysis

Using the method described by Li et al. (2019), the Sr, Mg, Ca, Mn, Fe, Al, and Si contents were measured at the Institute of the Earth Environment of the Chinese Academy of Sciences using a fourth-generation Avaatech high-resolution X-ray fluorescence (XRF) micro-core scanner. First, the stalagmite was fixed in the scanner to ensure that the profile of the stalagmite remained horizontal. Then, the surface of the stalagmite was cleaned with alcohol and covered with an ultra-thin film to prevent the sample from contaminating the detector during the analysis and from affecting the test results (Li et al., 2019). The test voltage of the instrument was set to 30 kV and 10 kV, the test current was 0.03 mA and 0.07 mA, the counting time was 10 s, the filter piece was made of Pd, and the testing dead time was about 30%. The scanning was conducted along the stalagmite's growth axis (Fig. 2A), the scanner radiation area was set as 2 mm × 2 mm, and the scanning resolution of RM8-2 was 0.1 mm. The results obtained from the XRF core scanning analysis are semi-quantitative and are reported as count rates (counts per second (cps), expressed as the number of units per unit time per unit area) (Francus P et al., 2009).

4. Results

4.1. XRD and SEM

The XRD results reveal that the sample collected from 25 mm is calcite, while the samples collected from 68 mm, 79 mm, 119 mm, 170 mm, and 220 mm are aragonite (Fig. S2). A similar profile suggests that the stalagmite is composed of aragonite at these other depths (Fig. 2A). This indicates that the gray section (19−30 mm, 1409−1169 yr BP) at the top of stalagmite SJJ7 is calcite (Figs. 2A and S2), while the other dark layers and light layers are aragonite.

As shown in the SEM image (Fig. 3), the dark aragonite layers are composed of larger particles (Fig. 3A and B) and have more numerous and larger pores than the light aragonite layers (Fig. 3C and D).

4.2. The U-Th chronology

The U−Th dating results for stalagmite SJJ7 are presented in Table 1. The ^{238}U contents of most of the dated samples (47/49) range from 3766 to 47541 ppb, but they are as low as 484 ppb and 384 ppb at depths of 25 mm and 28 mm from the top, respectively (Table 1). The U content of the calcite is far lower than that of the aragonite. This relationship is expected for calcite and aragonite (Domínguez-Villar et al., 2017). All of the age results are consistent with the growth sequence and are reliable, except for two dating results in the bottom of the stalagmite (Table 1). The two dating results at the bottom of the stalagmite exceeded the ages of the upper samples and the simulated age because there are manyclay impurities (Table 1, Fig. 2A). Thus, only the 240 mm record from the top to the bottom of stalagmite SJJ7 was considered in this study. The age model for stalagmite SJJ7 was established using the Mod-Age software (Fig. 2B) (Hercman and Pawlak, 2012). The results show that the 0−240 mm section of stalagmite SJJ7 grew during 3109−694 yr BP. The mean temporal resolutions of the $\delta^{18}O$ and $\delta^{13}C$ records of this section are 2.5 yr. The mean error of the 47
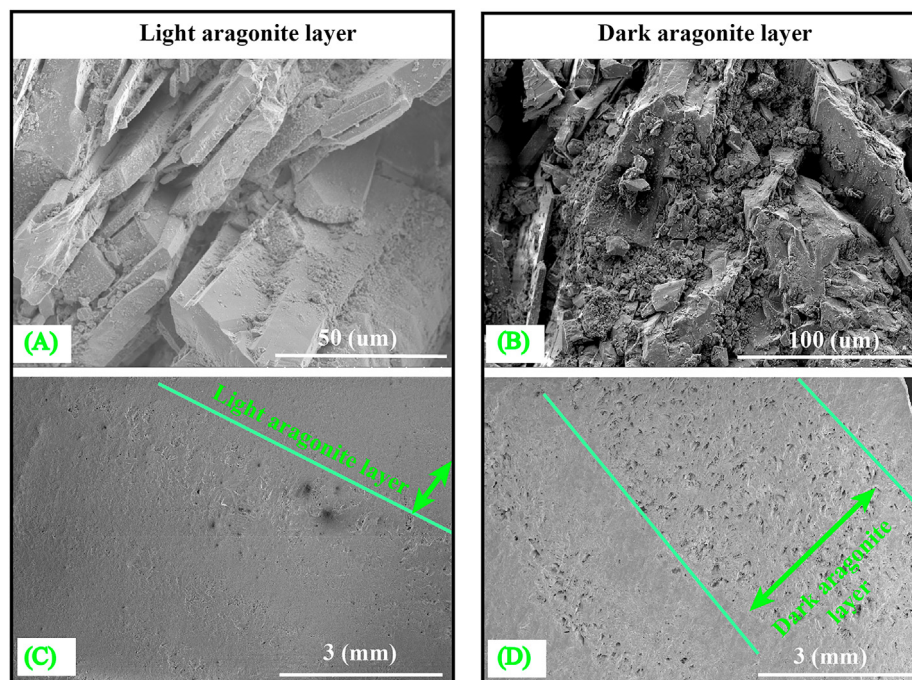
Fig. 3. SEM microphotograph of small slices of stalagmite SJJ7. (A) and (C) the light aragonite layers; and (B) and (D) the dark aragonite layers. Comparing (A) with (B), there are more large particles in the dark layers.

dating results is ± 14 yr.

4.3. $\delta^{18}O$ and $\delta^{13}C$

The $\delta^{18}O$ values of stalagmite SJJ7 range from $-7.9‰$ to $-6.0‰$, with a mean of $-7.0‰$. During 3109−694 yr BP, the $\delta^{18}O$ exhibited an overall positive trend (Fig. 4A). In addition, at ~779, 1013−911, 1282−1172, 1736−1638, 1961−1864, 2472−2375, 2931−2818, and 3050−3014 yr BP, the $\delta^{18}O$ values that are offset by an amplitude of 1−1.5‰ were labeled as events 1−8 (Fig. 4A). Events 2−8 lasted for 102, 110, 98, 97, 97, 113, and 36 years, respectively. The duration of event 1 is uncertain because of the end of the growth of stalagmite SJJ7.

The $\delta^{13}C$ values of stalagmite SJJ7 range from $-8.2‰$ to $1.1‰$, with a mean value of $-4.4‰$ (Fig. 4B). The overall changes in the $\delta^{13}C$ and $\delta^{18}O$ values of stalagmite SJJ7 are consistent, and they are significantly related (r = 0.53, p < 0.01, n = 959). When $\delta^{18}O$ is positive, $\delta^{13}C$ is also positive. However, unlike $\delta^{18}O$, the $\delta^{13}C$ was not only positive during the eight weak summer monsoon events listed above but also positive at 2980−2382, 2199−1515, and 1304−1000 yr BP, exhibiting a pattern of gradually becoming positive and slowly becoming negative (Fig. 4B).

4.4. Sr/Ca, Mg/Ca, Si, Al, Mn, and Fe

The Sr/Ca (counts/counts) ratios of stalagmite SJJ7 range from 0.55×10^{-3} to 4.64×10^{-3}, with a mean of 2.74×10^{-3}. The Mg/Ca (counts/counts) ratios range from 0 to 0.13×10^{-3}, with a mean of 0.04×10^{-3}. The Si contents (counts) range from 8.83 to 21.60, with a mean of 99.59. The Al (counts) contents range from 6.87 to 12.36, with a mean of 9.73. The Mn contents (counts) range from 8.83 to 21.60, with a mean of 13.22. The Fe contents (counts) range from 79.29 to 199.43, with a mean of 106.16. The high Sr/Ca $\times 10^3$ and Mg/Ca $\times 10^3$ ratios correspond to the positive $\delta^{18}O$ values, and the low Sr/Ca $\times 10^3$ and Mg/Ca $\times 10^3$ ratios correspond to the negative $\delta^{18}O$ values (Figs. 5 and S3). For example, during events 2 and 4−8,

the $\delta^{18}O$ values were positive, and the Sr/Ca $\times 10^3$ and Mg/Ca $\times 10^3$ ratios were higher. In particular, during the 1409−1169 yr BP period of calcite growth, the Sr/Ca $\times 10^3$ ratio was significantly lower, and the Mg/Ca $\times 10^3$ ratio increased significantly (Fig. 5C and D). The Savitzky−Golay (SG) smoothing tool in the Origin 9.1 software was used to smooth the Sr, Mg, Ca, Mn, Fe, Al, and Si results of 40 points, and then the results were compared with the $\delta^{18}O$ and $\delta^{13}C$ of SG smoothed 16 points. The Mn, Fe, Al, and Si contents of the dark layers (a−g) of the stalagmite are significantly higher and correspond to the stages when the $\delta^{18}O$ and $\delta^{13}C$ changed from negative to positive (Fig. 6). However, the Si, Al, and Fe contents of the calcite decreased while the Mn content increased (Fig. 6). The growth time of the 7 dark layers (a−g) occurred on an interdecadal scale (15−43 yr; Supplementary Table S1).

5. Discussion

5.1. Aragonite-calcite transition

The XRD results show that the stalagmite SJJ7 changed to calcite precipitation during 1409−1169 yr BP (19−30 mm; Figs. 2A and S2). The uranium concentration of the calcite decreased by two orders of magnitude, i.e., 21400.0 ppb and 47541.7 ppb at depths of 31 mm and 18 mm for the aragonite in stalagmite SJJ7, respectively, and 484.3 ppb and 384.9 ppb at depths of 25 mm and 28 mm for the calcite in stalagmite SJJ7, respectively (Table 1). This indicates that the calcite in stalagmite SJJ7 is the result of primary deposition rather than recrystallization because previous studies have shown that the uranium concentration of recrystallized calcite will not change significantly (Domínguez-Villar et al., 2017; Wassenburg et al., 2012). In addition, the formation of calcite via the recrystallization of aragonite will lead to disordered dating results (Fohlmeister et al., 2018). However, our precise dating results show that the two ages of the calcite conform to the stratigraphic order (Fig. 2B). Therefore, the calcite in stalagmite SJJ7 is primary. Furthermore, the transition from aragonite to calcite in stalagmites

Table 1
^{230}Th dating results for stalagmite SJJ7 from Shijiangjun cave in Guizhou, Southwest China. The errors are 2σ.

Sample	^{238}U		^{232}Th		^{230}Th/^{232}Th		δ^{234}U*		^{230}Th/^{238}U		^{230}Th Age (yr)		δ^{234}U$_{Initial}$**		^{230}Th Age (yr BP)***	
Number	(ppb)		(ppt)		(atomic x10^{-6})		(measured)		(activity)		(uncorrected)		(corrected)		(corrected)	
SJJ7-0.5	8183.7	±9.6	13244	±266	146	±3	738.0	±2.1	0.0143	±0.0002	902	±10	740	±2	**807**	**±22**
SSJ7-1.0	23047.9	±26.7	3432	±71	1765	±37	716.4	±1.8	0.0159	±0.0001	1017	±5	718	±2	**946**	**±5**
SJJ7-1.5	21639.2	±25.6	13265	±266	473	±10	739.9	±1.8	0.0176	±0.0001	1108	±4	742	±2	**1030**	**±8**
SJJ7-1.8	47541.7	±75.7	16367	±330	943	±19	721.7	±1.9	0.0197	±0.0001	1253	±4	724	±2	**1179**	**±6**
SJJ7-2.5	484.3	±0.4	1027	±21	170	±4	678.7	±1.6	0.0219	±0.0003	1431	±17	681	±2	**1326**	**±31**
SJJ7-2.8	384.9	±0.4	725	±15	204	±6	710.6	±2.0	0.0233	±0.0004	1493	±27	714	±2	**1393**	**±36**
SJJ7-3.1	21400.0	±32.8	7258	±147	1181	±24	742.6	±1.8	0.0243	±0.0001	1530	±6	746	±2	**1456**	**±7**
SJJ7-3.5	16004.6	±23.9	6685	±135	972	±20	746.2	±2.0	0.0246	±0.0001	1546	±7	749	±2	**1471**	**±9**
SJJ7-3.9	24076.1	±43.0	10583	±43	948	±6	754.2	±2.9	0.0253	±0.0001	1581	±9	758	±3	**1506**	**±10**
SJJ7-4.5	17129.9	±25.6	7698	±156	972	±20	758.2	±1.9	0.0265	±0.0001	1653	±9	762	±2	**1578**	**±10**
SJJ7-5.0	14291.2	±22.3	4344	±89	1527	±32	785.4	±2.1	0.0282	±0.0001	1732	±8	789	±2	**1659**	**±9**
SJJ7-5.5	13392.1	±18.2	11371	±228	561	±11	789.7	±2.1	0.0289	±0.0001	1771	±6	794	±2	**1689**	**±12**
SJJ7-6.2	12649.8	±19.9	838	±24	7284	±213	785.0	±2.0	0.0293	±0.0001	1801	±9	789	±2	**1732**	**±9**
SJJ7-6.8	11951.2	±15.1	1150	±26	5245	±120	835.9	±1.9	0.0306	±0.0001	1831	±7	840	±2	**1762**	**±7**
SJJ7-7.2	10548.6	±15.1	2401	±52	2261	±50	829.1	±2.1	0.0312	±0.0002	1874	±10	834	±2	**1802**	**±10**
SJJ7-7.7	8960.4	±11.2	4419	±90	1062	±22	828.1	±2.0	0.0318	±0.0001	1909	±9	833	±2	**1833**	**±11**
SJJ7-8.5	14392.8	±21.7	28443	±571	284	±6	824.0	±2.1	0.0340	±0.0001	2049	±7	829	±2	**1950**	**±23**
SJJ7-9.0	19306.1	±30.0	16478	±331	650	±13	798.9	±2.0	0.0337	±0.0001	2057	±6	804	±2	**1975**	**±12**
SJJ7-9.5	12523.5	±19.2	15437	±311	473	±10	833.3	±2.2	0.0354	±0.0002	2122	±10	838	±2	**2035**	**±17**
SJJ7-10.1	18262.8	±23.4	4151	±84	2541	±52	818.9	±1.9	0.0350	±0.0001	2117	±6	824	±2	**2046**	**±6**
SJJ7-10.7	14142.3	±21.9	26880	±540	311	±6	780.2	±2.2	0.0358	±0.0001	2212	±8	785	±2	**2114**	**±23**
SJJ7-11.0	28146.9	±49.9	3569	±73	4510	±92	719.2	±2.1	0.0347	±0.0001	2219	±6	724	±2	**2149**	**±6**
SJJ7-11.5	29951.2	±57.2	7463	±151	2298	±47	705.4	±2.2	0.0347	±0.0001	2240	±7	710	±2	**2168**	**±7**
SJJ7-11.9	15062.4	±16.7	955	±23	9734	±238	820.7	±1.8	0.0374	±0.0001	2263	±7	826	±2	**2194**	**±7**
SJJ7-12.5	15911.4	±21.0	8118	±164	1186	±24	748.4	±1.8	0.0367	±0.0001	2310	±7	753	±2	**2233**	**±9**
SJJ7-13.0	10776.1	±13.3	2000	±42	3250	±68	738.3	±2.0	0.0366	±0.0001	2316	±8	743	±2	**2245**	**±9**
SJJ7-13.5	14866.1	±21.0	3961	±81	2270	±47	719.5	±2.1	0.0367	±0.0001	2348	±8	724	±2	**2276**	**±8**
SJJ7-14.0	12626.0	±28.1	14975	±79	522	±5	712.2	±4.4	0.0375	±0.0003	2414	±21	717	±4	**2328**	**±23**
SJJ7-14.5	8554.3	±12.0	8060	±162	717	±15	819.7	±2.2	0.0410	±0.0001	2481	±7	825	±2	**2398**	**±13**
SJJ7-14.9	18477.9	±32.2	2290	±47	5513	±114	813.7	±2.3	0.0414	±0.0001	2517	±7	819	±2	**2447**	**±7**
SJJ7-15.2	5612.3	±5.9	8325	±167	473	±10	840.9	±2.0	0.0425	±0.0002	2545	±11	847	±2	**2454**	**±20**
SJJ7-15.7	12320.2	±17.3	5741	±117	1540	±32	845.0	±2.0	0.0435	±0.0001	2599	±9	851	±2	**2523**	**±10**
SJJ7-16.0	8382.2	±10.4	9564	±192	634	±13	841.5	±2.1	0.0439	±0.0002	2624	±11	848	±2	**2538**	**±17**
SJJ7-16.6	17506.6	±26.1	1544	±33	8218	±176	835.5	±2.2	0.0440	±0.0001	2640	±7	842	±2	**2570**	**±7**
SJJ7-17.0	11324.0	±12.9	5659	±114	1458	±30	822.8	±1.9	0.0442	±0.0001	2671	±7	829	±2	**2596**	**±9**
SJJ7-17.5	7974.3	±9.6	2461	±51	2392	±50	788.2	±2.0	0.0448	±0.0002	2760	±10	794	±2	**2687**	**±10**
SJJ7-18.2	18585.4	±25.3	2552	±52	5333	±110	771.3	±2.0	0.0444	±0.0001	2764	±7	777	±2	**2694**	**±7**
SJJ7-18.5	13457.9	±19.7	20182	±405	518	±10	828.2	±2.2	0.0471	±0.0001	2841	±8	835	±2	**2750**	**±19**
SJJ7-19.7	10174.8	±12.9	3094	±65	2608	±55	850.9	±2.1	0.0481	±0.0002	2865	±10	858	±2	**2793**	**±11**
SJJ7-20.2	12985.3	±18.5	3564	±73	2960	±61	859.3	±2.3	0.0493	±0.0001	2923	±9	866	±2	**2851**	**±9**
SJJ7-20.5	13607.6	±19.7	16260	±327	690	±14	866.2	±2.2	0.0500	±0.0001	2956	±9	873	±2	**2869**	**±16**
SJJ7-21.0	12944.8	±18.3	9785	±35	1082	±6	849.1	±2.8	0.0496	±0.00024	2958	±15	856	±2.8	**2880**	**± 16**
SJJ7-21.5	12529.0	±16.6	30984	±622	346	±7	872.6	±2.0	0.0519	±0.0001	3059	±9	880	±2	**2953**	**±29**
SJJ7-22.4	9551.4	±10.9	8189	±165	996	±20	862.7	±2.0	0.0518	±0.0001	3069	±9	870	±2	**2988**	**±13**
SJJ7-22.9	17799.5	±28.2	4192	±86	3605	±74	835.5	±2.2	0.0515	±0.0001	3097	±8	843	±2	**3025**	**±9**
SJJ7-23.5	15700.1	±25.0	43036	±864	315	±6	827.7	±2.1	0.0523	±0.0001	3160	±9	835	±2	**3049**	**±32**
SSJ7-24.2	9782.0	±14.5	51619	±1035	174	±4	873.5	±2.8	0.0556	±0.0002	3275	±12	881	±3	**3125**	**±59**
SSJ7-24.4	9140.1	±19.1	263180	±5292	41	±1	863.3	±3.4	0.0711	±0.0003	4230	±18	873	±3	**3714**	**±318**
SSJ7-24.8	5387.5	±16.1	1072966	±21677	31	±1	765.1	±5.6	0.3804	±0.0015	26005	±15	816	±8	**22704**	**±2296**

U decay constants: λ_{238} = 1.55125 × 10^{-10} (Jaffey et al., 1971) and λ_{234} = 2.82206 × 10^{-6} (Cheng et al., 2013). Th decay constant: λ_{230} = 9.1705x10-6 (Cheng et al., 2013). *δ^{234}U = ([^{234}U/^{238}U]$_{activity}$ − 1)x1000. **δ^{234}U$_{initial}$ was calculated based on ^{230}Th age (T), i.e., δ^{234}U$_{initial}$ = δ^{234}U$_{measured}$ x e$^{\lambda 234xT}$. Corrected ^{230}Th ages assume the initial ^{230}Th/^{232}Th atomic ratio of (4.4 ± 2.2) x10^{-6}. Those are the values for a material at secular equilibrium, with the bulk earth ^{232}Th/^{238}U value of 3.8. The errors are arbitrarily assumed to be 50%. ***B.P. stands for "Before Present" where the "Present" is defined as the year 1950 A.D.
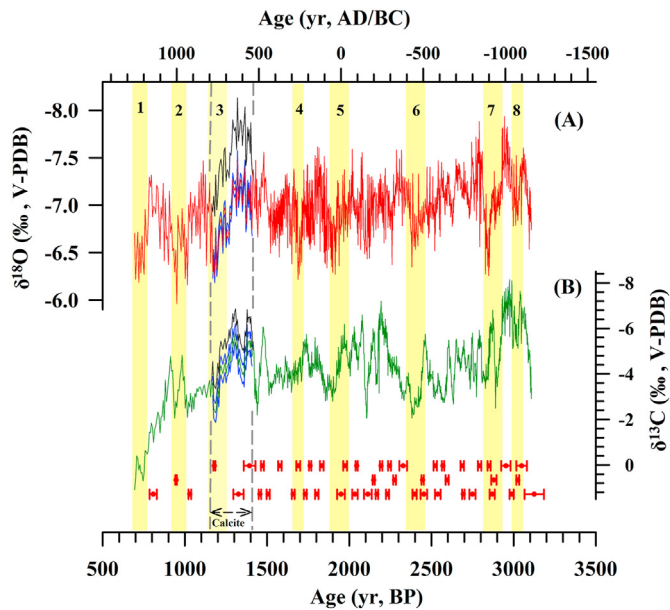
Fig. 4. Comparison of the $\delta^{18}O$ and $\delta^{13}C$ values of stalagmite SJJ7. (A) $\delta^{18}O$ record; (B) $\delta^{13}C$ record. The red error bars at the bottom show the dating points and the age errors. The dotted black curves are the original $\delta^{18}O$ and $\delta^{13}C$ records of the calcite deposition. In this study, the $\delta^{18}O$ and $\delta^{13}C$ of the calcite were corrected by $+0.63 \pm 0.07$‰ and $+1.07 \pm 0.41$‰, respectively (Section 5.1). The red and green curves are the corrected $\delta^{18}O$ and $\delta^{13}C$ records. The blue curves are the correction error. Yellow bands 1–8 represent the eight significant weak ASM events recorded by the $\delta^{18}O$ values of stalagmite SJJ7. (For interpretation of the references to colour in this figure legend, the reader is referred to the Web version of this article.)

Fig. 5. Comparison of the $\delta^{18}O$, $\delta^{13}C$, Sr/Ca, and Mg/Ca values of stalagmite SJJ7. (A) $\delta^{18}O$ and (B) $\delta^{13}C$ records (16-point SG smoothing). (C) Sr/Ca $\times 10^3$ ratio, which is influenced by calcite deposition. The Sr/Ca ratio during 1409−1169 yr BP is significantly lower, which affects the analysis of the amplitude of all of the data. Fig. S3 shows the Sr/Ca $\times 10^3$ ratios of the aragonite section (D) Mg/Ca $\times 10^3$ ratio. The Mg/Ca ratios increased during the weak summer monsoon events and were higher in the calcite section (C and D have 40-point SG smoothing). The dotted lines indicate the period of calcite deposition. Yellow bands 2−8 indicate the weak ASM events recorded by the $\delta^{18}O$ values of stalagmite SJJ7. (For interpretation of the references to colour in this figure legend, the reader is referred to the Web version of this article.)

may be attributed to changes in the chemical properties of the drip water, especially the pH and Mg/Ca values of the drip water (Wassenburg et al., 2012; Riechelmann et al., 2014). The saturation index of calcite decreases with increasing pH and Mg/Ca (Fohlmeister et al., 2018).

The fractionation coefficients for the stable oxygen and carbon isotopes are different during the depositional processes of aragonite and calcite (Tarutani et al., 1969; Scroxton et al., 2017). According to the results of simulation experiments (Tarutani et al., 1969; Kim et al., 2007), the $\delta^{18}O$ and $\delta^{13}C$ of calcite deviate from those of aragonite by -0.8‰ and -2.5‰, respectively. However, the simulation and experimental results differ from the actual offset observed in natural caves (Fohlmeister et al., 2018). Fohlmeister et al. (2018) found that $\Delta\delta^{18}O$ is related to the growth rate of the stalagmite during the aragonite-calcite transition. The $\delta^{18}O$ values of the calcite section in stalagmite SJJ7 (deposited during 1409−1169 yr BP) were corrected according to the formula provided by Fohlmeister et al. (2018):

$$\Delta\delta^{18}O\ [‰] = -0.00418(\pm 0.00141)*\text{growth rate }[\mu m/a] - 0.546(\pm 0.093). \quad (1)$$

Here, $\Delta\delta^{18}O$ is the offset of $\delta^{18}O$ during the aragonite-calcite transition. Growth rate is the depositional rate of the stalagmite. In this study, the growth rate of the calcite was determined to be 20.40816 $\mu m/a$, and $\Delta\delta^{18}O$ was calculated to be 0.63 ± 0.07‰. However, $\delta^{13}C$ was not related to the growth rate of the stalagmite, and $\Delta\delta^{13}C_{mean} = 1.07 \pm 0.41$‰ (Fohlmeister et al., 2018). Therefore, the measured $\delta^{18}O$ and $\delta^{13}C$ values were corrected by $+0.63 \pm 0.07$‰ and $+1.07 \pm 0.41$‰, respectively. The corrected results exhibited the same overall trends in $\delta^{18}O$ and $\delta^{13}C$ as the uncorrected results (Fig. 4), so they are still significantly correlated
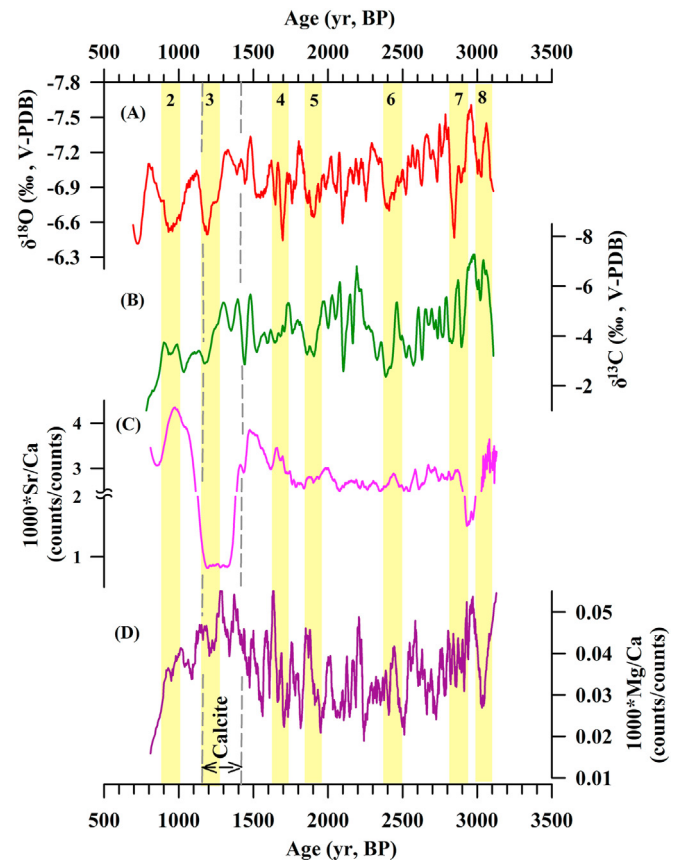
with each other ($r = 0.51$, $p < 0.01$, $n = 959$).

5.2. Significance of the stalagmite's $\delta^{18}O$

Many stalagmite records in the ASM region have been used to demonstrate that $\delta^{18}O$ reflects the intensity of the summer monsoon (Wang et al., 2005; Cosford et al., 2008; Kathayat et al., 2017; Tan et al., 2018). For example, the $\delta^{18}O$ of a stalagmite from DG cave reflected the intensity of the ASM on a centennial-millennial scale; that is, the stronger the ASM, the more negative the $\delta^{18}O$ of the stalagmite, and vice versa (Wang et al., 2005; Duan et al., 2014). Model simulation results have also shown that the $\delta^{18}O$ of stalagmites in the Asian monsoon region reflects the monsoon intensity (Liu et al., 2016). However, several studies have also shown that the $\delta^{18}O$ of stalagmites is affected by many factors, such as the cave temperature, rainfall, winter/summer rainfall ratio, water vapor source, water vapor transport path, and the condensation and evaporation of water vapor, which leads to controversial interpretations of stalagmite $\delta^{18}O$ values (Dayem et al., 2010; Li et al., 2018; Maher and Thompson, 2012; Pausata et al., 2011; Tan, 2014). The rainfall across central and eastern China mainly comes from the Indian Ocean (Baker et al., 2015). Part of the controversy arises from differences in our understanding of and definition of
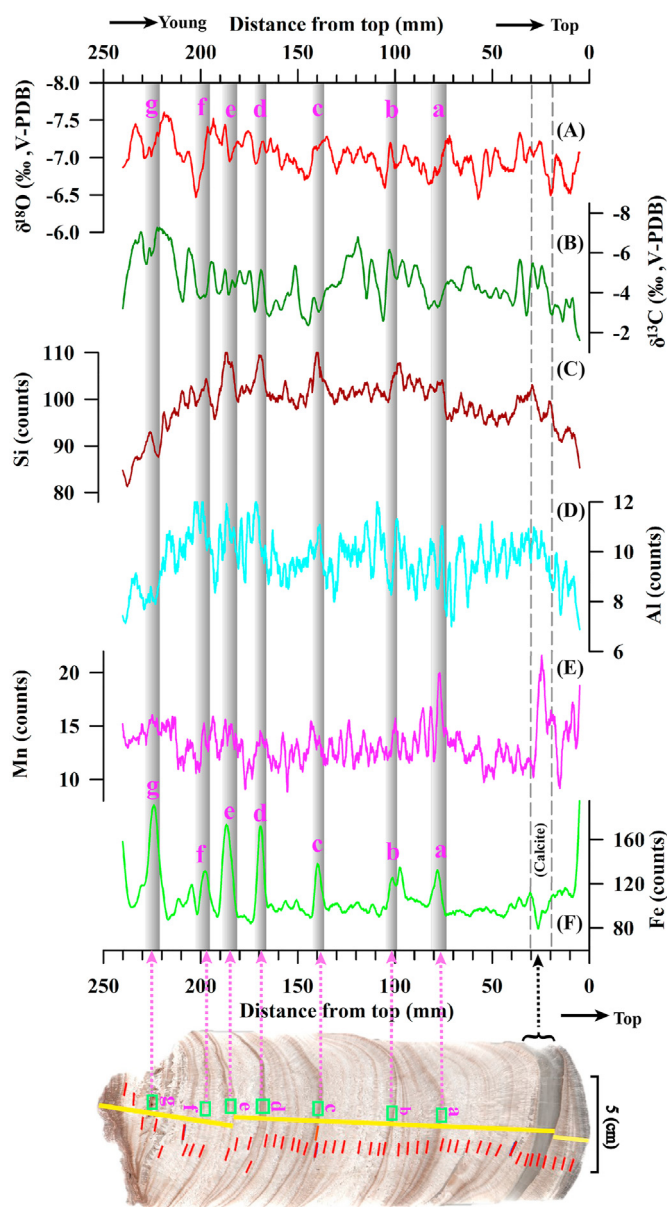
Fig. 6. Comparison of the Si, Al, Mn, and Fe contents and δ18O and δ13C of stalagmite SJJ7. (A) δ18O and (B) δ13C records (16-point SG Smoothing). (C–F) Si, Al, Mn, and Fe records (40-point SG Smoothing), respectively. The gray bands correspond to the dark layers in the stalagmite profile, and a–g are the seven dark layers in the stalagmite profile. The Si, Al, Mn, and Fe contents of the dark layers in the stalagmite exhibit pulsed increases. The dashed lines indicate the period of calcite deposition.
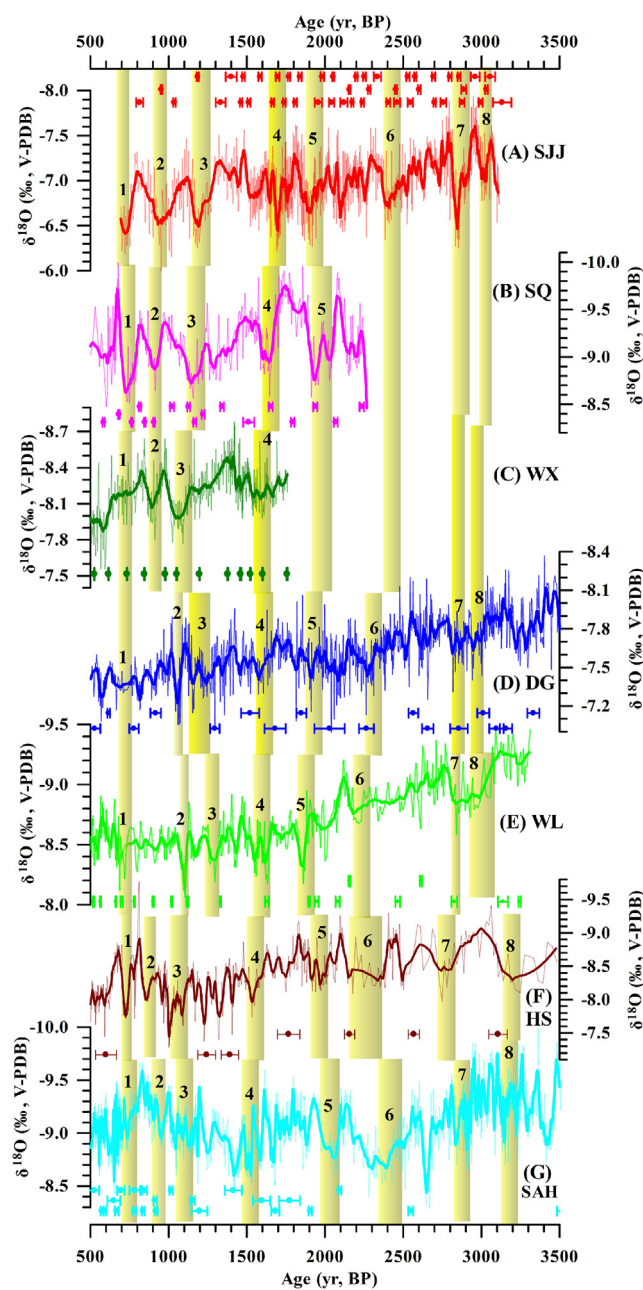

Fig. 7. Comparison of paleoclimate records in the Asian monsoon region during the Late Holocene. (A) SJJ Cave (this study); (B) SQ Cave (Tan et al., 2018); (C) WX Cave (Zhang et al., 2008); (D) DG Cave (Duan et al., 2014); (E) WL Cave (Zhao et al., 2020); (F) HS Cave (Hu et al., 2008); and (G) SAH Cave (Kathayat et al., 2017). The age points and errors are shown at the bottom of each record. The locations of each stalagmite record are shown in Fig. 1. Yellow bands 1–8 indicate the weak ASM events recorded by the δ18O values of stalagmite SJJ7. The light thin lines are the original δ18O records of each stalagmite; and the bold dark lines were smoothed using a 16-point SG. (For interpretation of the references to colour in this figure legend, the reader is referred to the Web version of this article.)

monsoon intensity (Cheng et al., 2019). The δ18O values of stalagmites are the cumulative result of the changes in the entire water vapor process from the water vapor source to the cave, and they do not indicate that rainfall mainly occurs in the water vapor path (Cheng et al., 2019). On the interdecadal−centennial scale, the δ18O values of stalagmites from the SQ Cave have been used to reconstruct changes in rainfall in Southwestern China since 2.30 ka BP. The rainfall changes determined are consistent with those reconstructed from pollen, tree rings, etc., for the southeastern part of the Qinghai Tibetan Plateau (Tan et al., 2018). This indicates that stalagmite δ18O values do reflect changes in rainfall on the interdecadal−centennial scale (Tan et al., 2018). Modern observational data have revealed that the δ18O of the rainfall in Guiyang is affected by the Asian monsoon, and thus, the δ18O of the rainfall is

lighter in the summer and heavier in the winter (Fig. S1). In addition, the modern monitoring results for SJJ Cave show that the δ18O of the drip water in the cave effectively recorded information about the local rainfall (Liu et al., 2008). In summary, we conclude that the δ18O of stalagmite SJJ7 can reflect the changes in the intensity of the ASM on the interdecadal−centennial scale. When the ASM was stronger, the δ18O of stalagmite SJJ7 was more negative, whereas when the ASM was weaker, the δ18O was more positive.

Determining whether the $\delta^{18}O$ of the stalagmite reflects changes in regional rainfall requires the analysis of multiple stalagmite proxies.

5.3. The changes in the ASM during the Late Holocene

5.3.1. Regional comparisons

The $\delta^{18}O$ record of stalagmite SJJ7 and other stalagmite records in the ASM region uniformly demonstrate that the ASM was weakened throughout the Late Holocene (Fig. 7), but there were differences in the internal variability of the different stalagmite $\delta^{18}O$ records on the interdecadal-centennial scale (Fig. 7). Tan et al. (2018) reconstructed a rainfall record for Southwestern China since 2.30 ka BP using the composite $\delta^{18}O$ records of stalagmites SQ 1 and SQ 7. The rainfall in Southwestern China decreased during weak summer monsoon events 1–5 (Tan et al., 2018). Although the high-precision records of stalagmites from the WX and SQ caves were shorter, they were well duplicated by stalagmite SJJ7 in the over-lapping time period (Fig. 7A−C). The $\delta^{18}O$ records of the stalagmites from DG (Duan et al., 2014) and WL caves (Zhao et al., 2020) in Southwestern China also recorded monsoon events 1−8 (Fig. 7C and D), despite variations in the magnitudes and phases of these events. Events 1−2 in the DG and WL caves records were not remarkable, while the records from other caves clearly recorded the sudden occurrences of these two events (Fig. 7). There are 50–150 yr phase differences for weak summer monsoon events 3, 4, 6, 7, and 8 between the $\delta^{18}O$ records of SJJ and HS caves in central China (Fig. 7E) (Hu et al., 2008). This may be due to uncertainties in the ages of the samples. The stalagmite record for HS Cave is controlled by only 8 dates, and its mean dating error is ±56 yr. The record for SJJ7 cave was more precise, with 47 high-precision dates and a mean error of ±14 yrr (Fig. 7A and E). Similarly, the change of the Indian summer monsoon (ISM), which was reconstructed using stalagmites from SAH Cave in Northern India (Kathayat et al., 2017), contained the same weak summer monsoon events (1−6) recorded by stalagmite SJJ7 (Fig. 7F). The obscure expression of events 7 and 8 in the SAH records may be due to the poorer age control of stalagmite SAH between 2500 and 3500 yr BP (Fig. 7F).

However, on the interdecadal-centennial timescale, these weak ASM events, which were recorded by two high-precision records from the same cave, are slightly different. For example, the $\delta^{18}O$ values of stalagmite DA from DG cave, which has a 4.5 yr resolution, have a phase difference of about 50−100 years, compared with the records for stalagmite DAS (3.5 yr resolution) from the same cave (Wang et al., 2005; Duan et al., 2014). Therefore, the differences in the dating errors and resolutions of the different stalagmite records may be the cause of the differences in the internal details of these weak summer monsoon events (Duan et al., 2014). The in-consistencies of these events may also be attributed to different factors such as the differences in hydrological routing, the degree of isotopic fractionation, the residence time during transport, differ-ences in the properties of the cracks, and the growth rate of the stalagmites (Cosford et al., 2008; Baker et al., 2015; Duan et al., 2014). Due to the advantages of a particularly high resolution (2.5 years), more precise dating, and accurate chronology (Fig. 7A), our new $\delta^{18}O$ records for stalagmite SJJ7 provide an opportunity to explore the ASM events during the Late Holocene in more detail.

In summary, the $\delta^{18}O$ records of stalagmite SJJ7 and other sta-lagmites in the ASM region indicate that the ASM has generally been decreasing since the Late Holocene. Furthermore, based on the unprecedented high resolution and high precision $\delta^{18}O$ record for stalagmite SJJ7, on the interdecadal-centennial timescale, the ASM decreased significantly at ~779, 1013−911, 1282−1172, 1736−1638, 1961−1864, 2472−2375, 2931−2818, and 3050−3014 yr BP (i.e., events 1−8, respectively). The multiple

Table 2
The Periods and Contribution rates (CRs) of the IMF and R. According to the methods of Wu and Huang (2009) and Yang et al. (2017), the analysis was conducted in Matlab.

	IMF1	IMF2	IMF3	IMF4	IMF5	IMF6	IMF7	IMF8	R
Period (yr)	**7**	15	32	75	181	294	648	1716	R
CR (%)	**36.8**	8.3	4.5	9.8	10.9	8.9	2.2	0.3	18.3

proxies used to analyze stalagmite SJJ7 present a possibility for further study of these climate events and any changes in the regional hydrological conditions (**Sections 5.4**−5.6).

5.3.2. Driving mechanism

The $\delta^{18}O$ record of stalagmite SJJ7 was decomposed into 8 sec-tions using the Intrinsic Mode Function (IMF1−IMF8) and a trend (R) using the Ensemble Empirical Mode Decomposition (EEMD) tool in Matlab (Fig. S4). In addition, the EEMD method was used to calculate their mean periods and contribution rates (Table 2) (Wu and Huang, 2009; Yang et al., 2017). The contribution rate can be used to accurately judge the influence of signals with different scales and to more effectively understand the driving mechanism of climate change (Yang et al., 2017). According to the results pre-sented in Table 2, the contribution rate of IMF1's 7 yr period is the largest (36.8%), which indicates that there is a significant El Niño-Southern Oscillation (ENSO) period (2−7 yr) in the $\delta^{18}O$ record of stalagmite SJJ7. The contribution rate of R is the second largest (18.3%), and R responds to the weak solar radiation on a sub-orbital scale (Figs. 8B and S4). From the decadal to centennial scales (Table 2), the periods (15−648 yr) can be related to the solar irra-diance and climatic feedbacks, which are linked to solar forcing (Wan et al., 2011). However, the millennial scale is also very feeble in the $\delta^{18}O$ record of stalagmite SJJ7 (Table 2).

The $\delta^{18}O$ records of stalagmite SJJ7 and other stalagmite records in the ASM region exhibit an overall positive trend during the Late Holocene (Fig. 7), indicating that the ASM gradually weakened as the solar radiation gradually decreased on the sub-orbital scale (Fig. 8B) (Cheng et al., 2016; Wan et al., 2011; Zhao et al., 2020). Although solar activity was an important external factor driving the changes in the ASM during the Late Holocene (Duan et al., 2014), the changes in the internal components of the climate system may be an internal factor that led to changes in the ASM on the interdecadal-centennial scale (Tan, 2016; Wang et al., 2017; Tan et al., 2019).

Previous studies have suggested that the ENSO is an interannual scale event (Conroy et al., 2008; Du et al., 2021). Why was the ENSO period dominant in the $\delta^{18}O$ record of stalagmite SJJ7 (Table 2)? First, many studies have shown that the activity of ENSO events increased significantly in the Late Holocene (Moy et al., 2002; Rein et al., 2005; Conroy et al., 2008; Toth et al., 2012; Zhang et al., 2014b; Carré et al., 2014; Du et al., 2021). Second, the northern-southern shift in the Intertropical Convergence Zone's (ITCZ's) po-sition also has an interdecadal-centennial scale cycle (Lechleitner et al., 2017; Tan et al., 2019), and the southward migration of the ITCZ may have caused the ENSO events to significantly increase, becoming El Niño-like on an interdecadal-centennial scale cycle (Du et al., 2021; Tan et al., 2019). The instrumental data indicate that the East Asian Summer Monsoon (EASM) weakened and the rainfall in Guiyang decreased during the El Niño events in the 1950−2004 yr AD period (Fig. S5). The opposite effect occurred when La Niña events occurred. The ITCZ has moved southward overall during the 20th century (Fig. S5A). The instrumental data show that the EASM weakened as the ITCZ moved southward during 1950−2004 yr AD (Fig. S5B) (Li and Zeng, 2003), and the
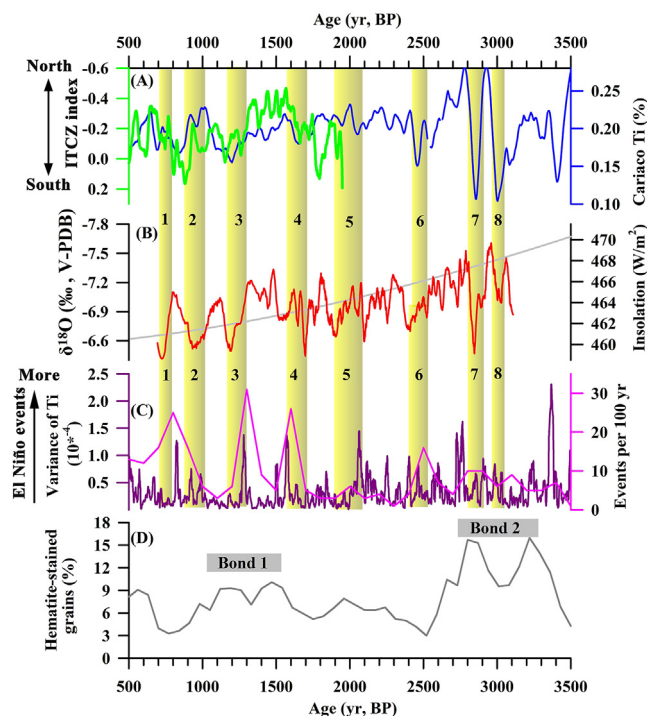
Fig. 8. Driving mechanism of the ASM during the Late Holocene. (A) The green curve is the index of the ITCZ (Tan et al., 2019). The blue curve is the Ti content in the Cariaco Basin (Haug et al., 2001); (B) The red curve is that of stalagmite SJJ7. The gray curve is the solar radiation in June–August at 65°N (Berger, 1978). (C) The pink curve is the El Niño events per 100 years (Moy et al., 2002). The purple curve is the variance in Ti in the Santa Barbara Basin (Du et al., 2021). (D) The hematite-stained grain (HSG) content of the North Atlantic (Bond et al., 2001). Yellow bands 1–8 are the weak ASM events recorded by the $\delta^{18}O$ values of stalagmite SJJ7. (For interpretation of the references to colour in this figure legend, the reader is referred to the Web version of this article.)

rainfall in Guiyang decreased overall (Fig. S5C). In the same period, the ISM also decreased (Yang et al., 2019). Therefore, the southward shift of the ITCZ and the stronger El Niño events may have driven these weak ASM events on the interdecadal-centennial scale.

The change in the Ti content in the Cariaco Basin indicates that the ITCZ dramatically shifted southward during events 3 and 6–8 (Fig. 8A) (Haug et al., 2001). The higher resolution ITCZ record for the past 2000 yr also indicates that the ITCZ shifted southward during events 1–5 (Fig. 8A). Moy et al. (2002) proposed that the activity of El Niño events per 100 years increased in the Late Holocene, especially during 2000–500 yr BP (Fig. 8C). The marine sediments in the Santa Barbara Basin also revealed that the occurrence of weak ASM events in the Late Holocene corresponded to periods with more frequent El Niño events (Fig. 8B and C). The tropical convective activity in low latitude areas provides the main source of water vapor and heat for the middle and high latitudes (Tan et al., 2019). The northern-southern shift in the ITCZ's position and the ENSO activity directly drive the changes in the tropical ocean areas and atmospheric circulation (Dong and Sutton, 2002; Moy et al., 2002; Wang et al., 2017; Tan et al., 2019). The northern-southern shifts in the ITCZ's position directly influence the amount of water vapor in the ASM (Dong and Sutton, 2002). When the ITCZ moves southward, the convection of the ascending branch of the Hadley circulation in the northern hemisphere weakens (Tan et al., 2019), resulting in weaker ASM events (Fig. 8A and B). The change in the amount of summer solar radiation in the Northern Hemisphere dominates the meridional temperature gradient between the Northern and Southern Hemispheres, causing shifts in the ITCZ (Schneider et al., 2014). Therefore, the northern-southern shift in

the ITCZ's position may be the result of feedback from the solar radiation signal, which affects the strength of the ASM. When an El Niño event occurs, the Walker Circulation weakens, and the ascending branch of the Walker Circulation in the Western Pacific Ocean moves eastward (Berkelhammer et al., 2014; Zhao et al., 2016). The warm surface water of the western pacific warm pool (WPWP) moves eastward, and the scope of the warm pool narrows, which leads to a decrease in the surface temperature of the WPWP and the westward movement of the stronger western pacific subtropical high (WPSH) (Zhao et al., 2016; Chen and Li, 2018). Therefore, the intensity of the ASM is suppressed (Wang et al., 2017; Chen and Li, 2018). This hypothesis has been confirmed through observations (Fig. S5). In addition, the weakening of the Atlantic meridional overturning circulation (AMOC) may result in a weak ASM due to the southward migration of the ITCZ (Haug et al., 2001; Wang et al., 2005; Cheng et al., 2016), which is supported by the good correlations between weak summer monsoon events 3 and 7–8, and Bond events 1 and 2, respectively (Fig. 8B and D).

5.4. $\delta^{13}C$

The $\delta^{13}C$ values of stalagmites are affected by atmospheric CO_2, soil, vegetation, the epikarst zone, and the cave conditions (temperature, humidity, and airflow) (Li et al., 2018). Previous studies have suggested that changes in the $\delta^{13}C$ of stalagmites reflect the distribution ratio of C_3 and C_4 plants under different climatic conditions (Dorale et al., 1998; McDermott, 2004). On the interdecadal-centennial scale, the $\delta^{13}C$ of stalagmites is mainly controlled by regional environmental changes, such as changes in vegetation coverage, soil microbial activities, and the regional hydrological cycle (Baker et al., 1997; Fairchild et al., 2006; Liu et al., 2016; Li and Li, 2018). Recently, studies of many monitored caves have determined that the $\delta^{13}C$ values of stalagmites can be used as a proxy for paleoclimate and for paleoenvironment reconstruction (Li et al., 2012; Oster et al., 2012). There is a significant correlation between the $\delta^{18}O$ and $\delta^{13}C$ values of stalagmite SJJ7 (R = 0.51, P < 0.01, n = 959). The cross-wavelet spectrum analysis of the $\delta^{18}O$ and $\delta^{13}C$ values of stalagmite SJJ7 revealed that they exhibit similar periods of 3–8, 10–15, 50–80, and 256–512 yr (Fig. 9). This is consistent with the $\delta^{18}O$ periods obtained from the EEMD analysis (Table 2), and the ENSO period marked in Fig. 9. Both the $\delta^{18}O$ and $\delta^{13}C$ values were significantly positive during events 1–8 (Fig. 4). This suggests that the $\delta^{13}C$ of stalagmites is closely related to the changes in the ASM on the interdecadal-centennial scale. The ASM and the regional rainfall decreased, resulting in a decrease in the vegetation coverage and soil microbial activity. Then, the prior calcite precipitation (PCP)/prior aragonite precipitation (PAP) increased in the karst zone, the water drop rate decreased, and the CO_2 degassing increased, which resulted in an increase in the $\delta^{13}C$ of the stalagmite (Tan et al., 2015; Li et al., 2018). The $\delta^{13}C$ values of stalagmite SJJ7 differed from its $\delta^{18}O$ during three periods: 2980–2382, 2199–1515, and 1304–1000 yr BP. The $\delta^{13}C$ values gradually became more positive, and then they slowly became negative (Fig. 4B). This may indicate that the deterioration and restoration of the ecological environment are slow processes that responded to climate change. In addition, after 0.80 ka BP, the $\delta^{13}C$ anomaly was positive. The tufa study in the Xiangshuihe River Basin in the same area also found a positive $\delta^{13}C$ anomaly in the same period (Liu et al., 2011). This may be due to the frequent human activities that occurred during this period, which aggravated the rocky desertification in this area (Liu et al., 2011). Expansion of the rocky desertification would lead to degradation of the surface vegetation, soil loss, and a reduction in soil CO_2, which would lead to a positive $\delta^{13}C$ anomaly in the stalagmites (Liu et al., 2011; Tan et al., 2015).
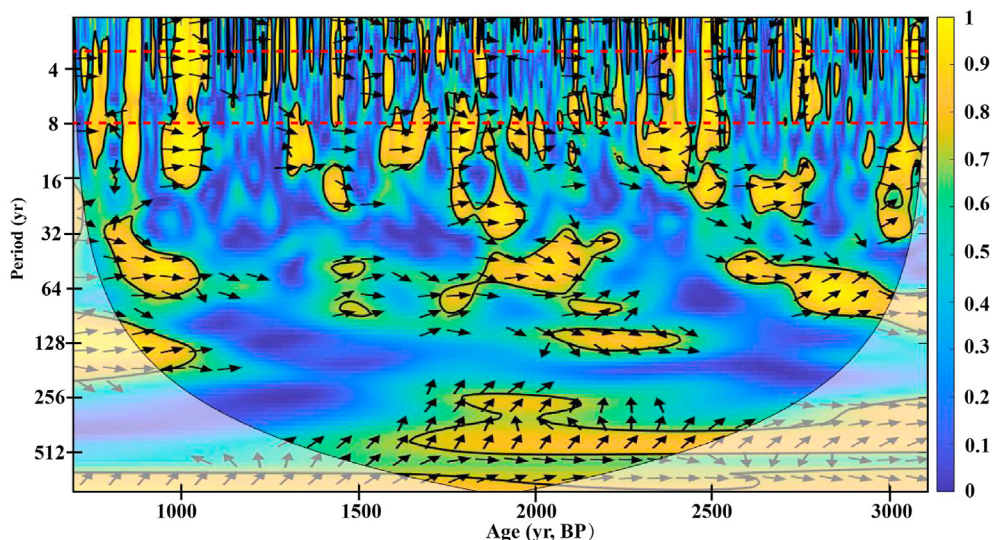
Fig. 9. The cross-wavelet spectrum between $\delta^{18}O$ and $\delta^{13}C$ for stalagmite SJJ7. According to the method of Grinsted et al. (2004), the analysis was conducted in Matlab (with in-phase pointing right, anti-phase pointing left). The area between the red dotted lines is the ENSO period. (For interpretation of the references to colour in this figure legend, the reader is referred to the Web version of this article.)

In summary, the $\delta^{18}O$ and $\delta^{13}C$ records of stalagmite SJJ7 are positively correlated. When the ASM was stronger, the stalagmite's $\delta^{18}O/\delta^{13}C$ ratios were negative; and when the ASM was weaker, the $\delta^{18}O/\delta^{13}C$ ratios were positive. We suggest that the $\delta^{18}O$ and $\delta^{13}C$ records of stalagmite SJJ7 reflect changes in the ASM, which were driven by the occurrence of more frequent ENSO events on the interdecadal-centennial scale.

5.5. Sr/Ca and Mg/Ca

The Mg/Ca and Sr/Ca ratios of stalagmites have been used as indicators of paleoclimate (Griffiths et al., 2010; Liu et al., 2013; Zhang et al., 2018). Zhang et al. (2018) reconstructed the rainfall changes in regions in central China during the last glacial maximum using the $\delta^{18}O$, $\delta^{13}C$, Mg/Ca, and Sr/Ca values of stalagmites from Haozhu Cave. The Mg/Ca and Sr/Ca ratios increased when the regional rainfall decreased in the Asian monsoon region (Johnson et al., 2006; Liu et al., 2013; Tan et al., 2018). Modern cave monitoring has provided reliable evidence that as rainfall decreases, the Mg/Ca and Sr/Ca ratios of cave drip water increase, and as rainfall increases, the Mg/Ca and Sr/Ca ratios decrease (Chen and Li, 2018).

The main part of stalagmite SJJ7 is composed of aragonite with a low Mg content, so the Mg/Ca ratio is lower than the Sr/Ca ratio. The Mg/Ca and Sr/Ca ratios increased, and the $\delta^{18}O$ and $\delta^{13}C$ were more positive (Figs. 5 and S3), corresponding to weak ASM events 2 and 4−8. When the rainfall decreased, more Mg and Sr were dissolved, and the residence time of the transport and the water-rock interactions increased (Johnson et al., 2006). CO_2 degassing and PCP/PAP increased in the karst zone, resulting in an increase in the Sr/Ca and Mg/Ca ratios of the stalagmites (Liu et al., 2013; Chen and Li, 2018; Zhang et al., 2018). By contrast, when the rainfall increased and the water-rock interactions decreased, the dissolution of Mg and Sr decreased. Then, the increased rainfall also inhibited the PCP/PAP, leading to a decrease in the Sr/Ca and Mg/Ca ratios of the stalagmites (Karmann et al., 2007; Wong et al., 2011).

However, the composition of stalagmite SJJ7 changed from aragonite to calcite, and the Sr/Ca and Mg/Ca ratios exhibited opposite trends during 1409−1169 yr BP (Fig. 5C and D). The Mg/Ca ratio increased and the Sr/Ca ratio rapidly decreased (Fig. 5C). Due to the different crystal structures of aragonite and calcite, the

partition coefficients (D (Mg), D (Sr)) of the trace elements in the stalagmite are very different: $D_{aragonite}$ (Mg)≪1, $D_{aragonite}$ (Sr) > 1; and $D_{calcite}$ (Mg)>$D_{aragonite}$ (Mg) and $D_{calcite}$ (Sr)<$D_{aragonite}$ (Sr) (Wassenburg et al., 2016). Compared to aragonite, the Mg/Ca ratios increased and the Sr/Ca ratios decreased in calcite (Baldini et al., 2012; Wassenburg et al., 2016). This is due to the fact that the smaller Mg ions tend to preferentially enter the calcite's triangular crystal lattice, while the larger Sr ions tend to preferentially enter the rhombic crystalline structure of aragonite (Wassenburg et al., 2012). Thus, Sr is incorporated into aragonite more easily than Mg (Reeder et al., 2000; Wassenburg et al., 2012; Vansteenberge et al., 2019). This is also the reason why the Mg content of stalagmite SJJ7 is much lower than the Sr content. Wassenburg et al. (2012) suggested that humid climates are favorable to calcite precipitation, whereas dry climates led to aragonite nucleation (Mcmillan et al., 2005). The early period (1409−1300 yr BP) of calcite deposition in stalagmite SJJ7 was characterized by a humid climate (strong ASM), but the later period of calcite deposition was characterized by a dry climate (weak ASM) (Figs. 4 and 5). The deposition of aragonite began again after event 3 (Figs. 2A and 4). The aragonite-calcite transition may be related to the Mg concentration of the drip water (Wassenburg et al., 2012). This is still unclear and is worthy of further study because modern cave monitoring results show that a high relative humidity in caves is beneficial to aragonite deposition (Rossi and Lozano, 2016).

In summary, although the Mg/Ca and Sr/Ca ratios of the aragonite-calcite transition in stalagmites are complex, their ratios in stalagmites sensitively respond to regional hydrological changes (Wassenburg et al., 2016, 2020). Moreover, when there is a change in the mineral composition of the stalagmites, careful interpretation is needed to determine the paleoclimate.

5.6. The dark layers of the stalagmite reflect a summer monsoon transition event

There are seven obvious dark layers (Fig. 2A) in the profile of stalagmite SJJ7. The XRD results indicate that these dark layers are aragonite deposits (Fig. S2). Similar dark layers have also been found in other stalagmites in many previous studies, for example, stalagmites from Lianhua Cave in Hunan Province (Cosford et al.,
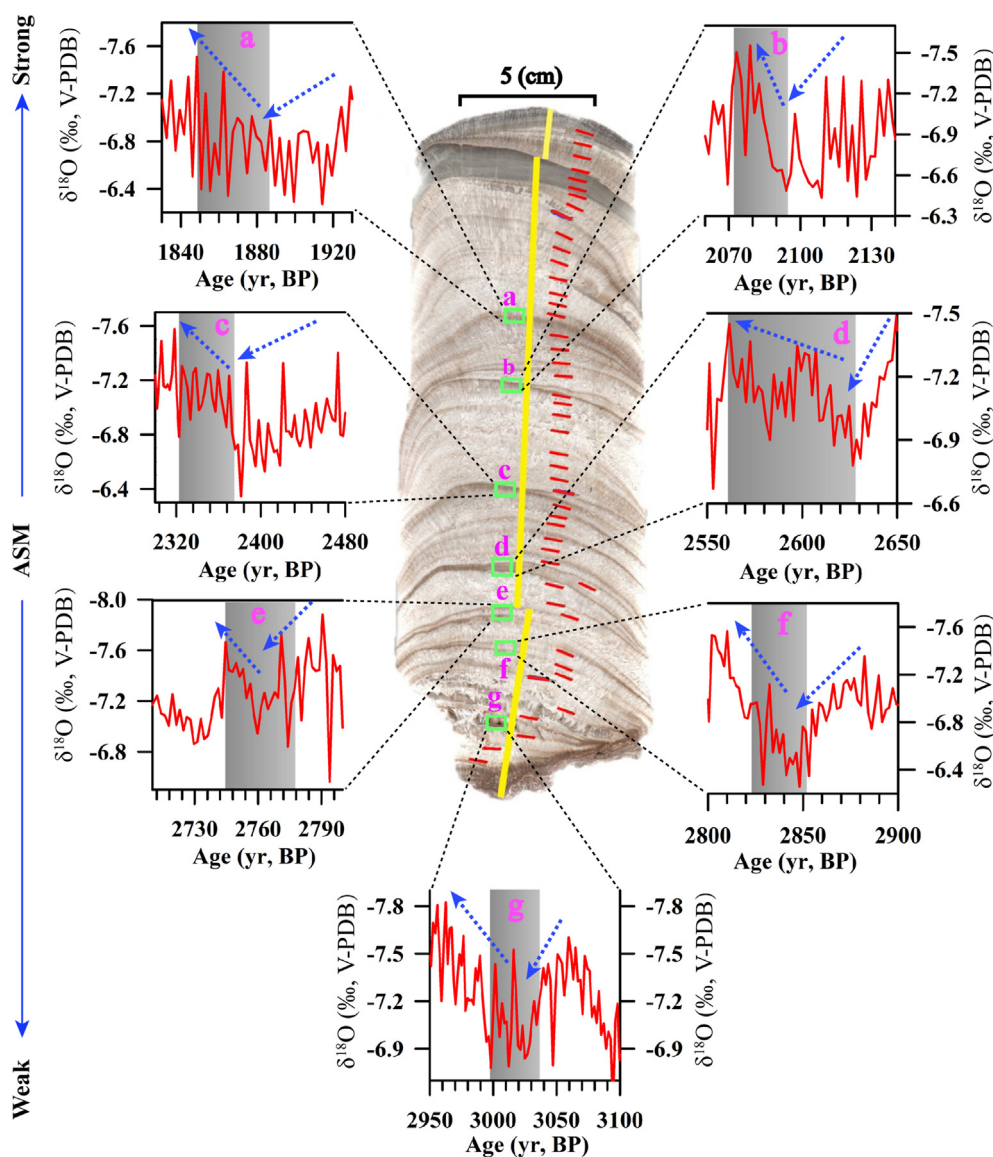
Fig. 10. Detailed comparison of the dark layers and δ^{18}O values. The gray bands in panes a–g are the periods in which the dark layers were deposited. The dark layers were deposited during the transition from heavy to light δ^{18}O values.

2008), Tianmen Cave in Tibet (Cai et al., 2012), and Lianhua Cave in Shanxi Province (Dong et al., 2015). However, these studies lacked a discussion of the dark layers in these stalagmites, and the climatic and environmental significances of the dark layers are still unclear.

Through the analysis of the concentrations of various elements in stalagmite SJJ7, it was found that the Si, Al, Mn, and Fe contents in the dark aragonite layers (a–g) in the stalagmite exhibit pulsed increases (Fig. 6) and reach a peak. These peaks are related to episodes of high rainfall and infiltration (Borsato et al., 2007). The interdecadal deposition of these dark aragonite layers (a–g) also corresponds to the transition from heavy to light δ^{18}O and δ^{13}C values (Fig. 10). When the weak ASM transitioned to strong ASM, the concentrations of these elements changed from a gentle fluctuation to a sudden increase, forming a peak. The peak characteristics of the Mn pulse are not obvious, but the Mn content increased during the monsoon transition events (Fig. 6E). Therefore, the dark aragonite layers (a–g) in stalagmites SJJ7 represent extreme changes in the regional hydrological environment, which may indicate a transitional period from weak ASM to strong ASM on the

interdecadal scale. The similar changes in Si, Al, Mn, and Fe indicate that they share the same deposition mechanism (Belli et al., 2017).

Unlike the dissolved phases of Ca, Mg, and Sr in the drip water, the colloid or particle forms of Si, Al, Mn, and Fe migrated through the soil and bedrock with the seasonal rainfall and finally appeared in the drip water (Baldini et al., 2012; Belli et al., 2017). The Si, Al, Mn, and Fe in the stalagmite primarily originated from the clay minerals in the soil (e.g., kaolinium, montmorillonite, chlorite, and illite) and soil organic matter (Hartland et al., 2011; Wassenburg et al., 2012; Belli et al., 2017; Dill, 2020). Clay minerals are a mixture of carbonate and silicate rock particles with particle sizes of less than 2 μm (Dill, 2020). Compared with the light aragonite layers, the dark aragonite layers have larger pores and coarser grains (Fig. 3), reflecting the rapid coagulation of clay minerals and their amorphous mineral colloids (Borsato et al., 2007; Schwertmann, 1971; Vansteenberge et al., 2019). The Fe content of the dark layers exhibits pulses (Fig. 6F), indicating the presence of abundant clastic materials (Vansteenberge et al., 2019). The migration of colloids and particles required sufficient mechanical

power (Richter et al., 2004; Zhou et al., 2008; Wassenburg et al., 2012). SJJ Cave is located under an isolated residual hill (Fig. 1B) (Duan et al., 2015), so rainfall is the main source of its groundwater and is the main power source for the transportation of colloidal and particulate materials. The changes in the stalagmite's $\delta^{18}O$ values from heavy to light indicate the strengthening of the ASM and an increase in rainfall (Figs. 9 and S6), which resulted in the strengthening of the mechanical power of the water in the soil and bedrock, which made it possible for the small soil particles to pass through the infiltration passageways and crannies (Vansteenberge et al., 2019). Finally, these elements were deposited on the surface of the stalagmite by the drip water, resulting in the pulsed increases in the clay mineral elements (e.g., Si, Al, Mn, and Fe) (Figs. 6 and S6).

In addition, the decreases in the Si, Al, and Fe contents of the calcite may be due to the different adsorption potentials of calcite and aragonite (Wassenburg et al., 2012). Compared with the sparse fibrous aragonite crystals, the compact columnar crystal structure of calcite inhibits the incorporation of these particle-associated elements (Domínguez-Villar et al., 2017; Vansteenberge et al., 2019). However, the increase in the Mn content of the calcite is attributed to the competition effects for the crystal defect sites (Wassenburg et al., 2012). Thus, these dark aragonite layers record a transition from weak ASM to strong ASM and changes in the regional hydrology. However, these elements may exhibit different changes in different soils and hydrological environments (Baldini et al., 2012). The implications of these elements need to be studied further in combination with cave monitoring data.

6. Conclusions

This study is based on high-precision U−Th dating and multiple proxies, which were used to analyze the $\delta^{18}O$, $\delta^{13}C$, Sr/Ca, Mg/Ca, Mn, Fe, Al, and Si values of stalagmite SJJ7 from Southwestern China. The high-resolution (2.5 years) record was reconstructed to investigate the history of the ASM during the Late Holocene (3109−694 yr BP). During this period, overall, the ASM experienced a weakening trend in response to the weaker solar radiation on a sub-orbital scale. There were eight weak summer monsoon events on the interdecadal-centennial scale, which occurred at ~779, 1013−911, 1282−1172, 1736−1638, 1961−1864, 2472−2375, 2931−2818, and 3050−3014 yr BP. Although there are differences in the details of the records of stalagmite SJJ7 and other stalagmites in the ASM region, the $\delta^{18}O$ record of stalagmite SJJ7 more accurately reflects the 8 weak ASM events during the Late Holocene. The cross-wavelet spectrum analysis of the $\delta^{18}O$ and $\delta^{13}C$ records of stalagmite SJJ7 indicates that they had similar periods (3−8, 10−15, 50−80, and 256−512 yr). The 7 yr period of the $\delta^{18}O$ records had the largest contribution rate (36.8%) to the periods based on EEMD analysis. On the interdecadal-centennial scale, the northern-southern shifts in the ITCZ's position may have been caused by feedback from the solar radiation signal. The southward migration of the ITCZ resulted in more El Niño events, and the high frequency of El Niño events dominated the weak monsoon events in the Late Holocene.

The $\delta^{13}C$ values of the stalagmite changed relatively slowly compared to the $\delta^{18}O$ values, which may indicate that the degradation and restoration of the regional ecological environment resulting from abrupt climate change is a relatively slow process. When the summer monsoon weakened, the Mg/Ca and Sr/Ca ratios of the stalagmite were relatively high because the CO_2 degassing and PCP/PAP increased in the karst zone. However, the Mg/Ca ratios increased and the Sr/Ca ratios rapidly decreased during the calcite deposition because of the differences in the crystal structures and partition coefficients of aragonite and calcite. Thus, the Mg/Ca and

Sr/Ca ratios of stalagmites sensitively respond to regional hydrological changes. The dark layers in stalagmite SJJ7 correspond to the transition from heavy to light $\delta^{18}O$ values, which is consistent with the transition in the ASM on an interdecadal timescale. The pulsed increases in the particle- and colloid-associated elements (e.g., Mn, Fe, Al, and Si) in the dark layers reflect the stronger mechanical power of the transport caused by more rainfall. Therefore, the changes in the ASM regulated the changes in the regional hydrological conditions and ecological environment and the element migration in the critical karst zones during the Late Holocene. The changes in paleoclimate and paleoenvironment were recorded by multiple proxies in the stalagmites.

Declaration of competing interest

The authors declare that they have no known competing financial interests or personal relationships that could have appeared to influence the work reported in this paper.

Appendix A. Supplementary data

Supplementary data to this article can be found online at https://doi.org/10.1016/j.quascirev.2021.106865.

Author contributions

T.-Y Li and J.-Y Li designed the research and revised the manuscript. C.-J. Chen and R Huang wrote the first version of the manuscript. J. Zhang., D.-X. Yuan, X.-Y. Long., T. Wang., S.-Y Xiao. and Y. Wu. contributed to oxygen isotope measurements and the [230]Th dating work. H. Cheng, C.-C Shen, Y.-F Ning and R. Lawrence Edwards provided technical support in [230]Th dating work. All authors discussed the results and provided ideas to input the manuscript.

References

Baker, A., Ito, E., Smart, P.L., Mcewan, R.F., 1997. Elevated and variable values of ^{13}C in speleothems in a British cave system. Chem. Geol. 136, 263−270.

Baker, A., Sodemann, H., Baldini, J., Breitenbach, S., Johnson, K., Van Hunen, J., 2015. Seasonality of westerly moisture transport in the east asian summer monsoon and its implications for interpreting precipitation $\delta^{18}O$. J. Geophys. Res. Atmos. 120.

Baldini, J.U.L., Mcdermott, F., Baldini, L.M., Ottley, C.J., Linge, K.L., Clipson, N., 2012. Identifying short-term and seasonal trends in cave drip water trace element concentrations based on a daily-scale automatically collected drip water dataset. Chem. Geol. 330−331.

Belli, R., Borsato, A., Frisia, S., Drysdale, R.N., Maas, R., Greig, A., 2017. Investigating the hydrological significance of stalagmite geochemistry (Mg, Sr) using Sr isotope and particulate element records across the Late Glacial-to-Holocene transition. Geochem. Cosmochim. Acta 199 (199), 247–263.

Berger, A.L., 1978. Long-term variations of caloric insolation resulting from the earth's orbital elements. Quat. Res. 9, 139–167.

Berkelhammer, M., Sinha, A., Mudelsee, M., Cheng, H., Yoshimura, K., Biswas, J., 2014. On the low-frequency component of the ENSO-Indian monsoon relationship: a paired proxy perspective. Clim. Pol. 10, 733–744.

Bond, G., Kromer, B., Beer, J., Muscheler, R., Evans, M.N., Showers, W., Hoffmann, S., Lotti-Bond, R., Hajdas, I., Bonani, G., 2001. Persistent solar influence on North Atlantic Holocene and glacial climates. Science 294, 2130–2136.

Borsato, A., Frisia, S., Fairchild, I.J., Somogyi, A., Susini, J., 2007. Trace element distribution in annual stalagmite laminae mapped by micrometer-resolution X-ray fluorescence: implications for incorporation of environmentally significant species. Geochem. Cosmochim. Acta 71 (6), 1494–1512.

Cai, Y.J., Zhang, H.W., Cheng, H., An, Z.S., Edwards, R.L., Wang, X.F., Tan, L.C., 2012. The Holocene Indian monsoon variability over the southern Tibetan Plateau and its teleconnections. Earth Planet Sci. Lett. 335-336, 135–144.

Carré, M., Sachs, J.P., Purca, S., Schauer, A.J., Braconnot, P., Angeles Falcon, R., et al., 2014. Holocene history of ENSO variance and asymmetry in the eastern tropical Pacific. Science 345 (6200), 1045–1048.

Chen, C.-J., Li, T.-Y., 2018. Geochemical characteristics of cave drip water respond to ENSO based on a 6-year monitoring work in Yangkou Cave, Southwest China. J. Hydrol. 561, 896–907.

Cheng, H., Edwards, R.L., Shen, C.-C., Polyak, V.J., Asmerom, Y., Woodhead, J., Hellstrom, J., Wang, Y., Kong, X., Spötl, C., 2013. Improvements in ^{230}Th dating, ^{230}Th and ^{234}U half-life values, and U-Th isotopic measurements by multi-collector inductively coupled plasma mass spectroscopy. Earth Planet Sci. Lett. 82–91.

Cheng, H., Edwards, R.L., Sinha, A., Spotl, C., Yi, L., Chen, S., et al., 2016. The Asian monsoon over the past 640,000 years and ice age terminations. Nature 534 (7609), 640–646.

Cheng, H., Zhang, H., Zhao, J., Li, H., Ning, Y., Kathayat, G., 2019. Chinese stalagmite paleoclimate researches: a review and perspective. Sci. China Earth Sci. 1–25.

Conroy, J.L., Hudson, A.M., Overpeck, J.T., Liu, K.-B., Wang, L., Cole, J.E., 2017. The primacy of multidecadal to centennial variability over late-Holocene forced change of the Asian Monsoon on the southern Tibetan Plateau. Earth Planet Sci. Lett. 458, 337–348.

Conroy, J.L., Overpeck, J.T., Cole, J.E., Shanahan, T.M., Steinitz-Kannan, M., 2008. Holocene changes in eastern tropical Pacific climate inferred from a Galápagos lake sediment record. Quat. Sci. Rev. 27 (11–12), 1166–1180.

Cook, E.R., Anchukaitis, K.J., Buckley, B.M., D'Arrigo, R.D., Jacoby, G.C., Wright, W.E., 2010. Asian monsoon failure and megadrought during the last millennium. Science 328, 486–489.

Cosford, J., Qing, H., Eglington, B., Mattey, D., Yuan, D., Zhang, M., Cheng, H., 2008. East Asian monsoon variability since the Mid-Holocene recorded in a high-resolution, absolute-dated aragonite speleothem from eastern China. Earth Planet Sci. Lett. 275, 296–307.

Cruz Jr., F.W., Burns, S.J., Jercinovic, M., Karmann, I., Sharp, W.D., Vuille, M., 2007. Evidence of rainfall variations in Southern Brazil from trace element ratios (Mg/Ca and Sr/Ca) in a Late Pleistocene stalagmite. Geochem. Cosmochim. Acta 71, 2250–2263.

Dasgupta, S., Saar, M.O., Edwards, R.L., Shen, C.-C., Cheng, H., Alexander Jr., E.C., 2010. Three thousand years of extreme rainfall events recorded in stalagmites from Spring Valley Caverns, Minnesota. Earth Planet Sci. Lett. 300, 46–54.

Dayem, K.E., Molnar, P., Battisti, D.S., Roe, G.H., 2010. Lessons learned from oxygen isotopes in modern precipitation applied to the interpretation of speleothem records of paleoclimate from eastern Asia. Earth Planet Sci. Lett. 295, 219–230.

Dill, H.G., 2020. A geological and mineralogical review of clay mineral deposits and phyllosilicate ore guides in central Europe a function of geodynamics and climate change. Ore Geol. Rev. 119, 103304.

Domínguez-Villar, David, Krklec, Kristina, Pelicon, Primo, Fairchild, Ian J., Cheng, Hai, Edwards, Lawrence R., 2017. Geochemistry of speleothems affected by aragonite to calcite recrystallization–potential inheritance from the precursor mineral. Geochem. Cosmochim. Acta 200, 310–329.

Dong, J.G., Shen, C.C., Kong, X.G., Wang, H.C., Jiang, X.Y., 2015. Reconciliation of hydroclimate sequences from the Chinese Loess Plateau and low-latitude East Asian Summer Monsoon regions over the past 14,500 years. Palaeogeogr. Palaeocl. 435, 127–135.

Dong, B.W., Sutton, R.T., 2002. Adjustment of the coupled ocean-atmosphere system to a sudden change in the thermohaline circulation. Geophys. Res. Lett. 29 (15), 18-1.

Dorale, J.A., Edwards, R.L., Ito, E., González, L.A., 1998. Climate and vegetation history of the midcontinent from 75 to 25 ka: a speleothem record from crevice cave, Missouri, USA. Science 282, 1871–1874.

Duan, F., Wang, Y., Shen, C.C., Wang, Y., Cheng, H., Wu, C.C., Zhao, K., 2014. Evidence for solar cycles in a late Holocene speleothem record from Dongge Cave, China. Sci. Rep. 4, 5159.

Du, X.J., Hendy, I., Hinnov, L., Brown, E., Zhu, J., Poulsen, C.J., 2021. High-resolution interannual precipitation reconstruction of Southern California: Implications for Holocene ENSO evolution. Earth Planet Sci. Lett. 554, 116670.

Duan, Y.F., Liu, Z.Q., He, Q.F., Lv, X.F., Jiang, J.J., 2015. Geochemistry of drip water in cave of rocky areas—A case study of Shijiangjun cave in Guizhou Province. J. South China Normal Univ. (Soc. Sci. Ed.) 40 (4), 95–101 (in Chinese with English abstract).

Edwards, R.L., Chen, J.H., Wasserburg, G.J., 1987. ^{238}U-^{234}U-^{230}Th-^{232}Th systematics and the precise measurement of time over the past 500,000 years. Earth Planet Sci. Lett. 81, 175–192.

Fairchild, I.J., Smith, C.L., Baker, A., Fuller, L., Spotl, C., Mattey, D., McDermott, F., Eimp, 2006. Modification and preservation of environmental signals in speleothems. Earth Sci. Rev. 75, 105–153.

Fairchild, I.J., Treble, P.C., 2009. Trace elements in speleothems as recorders of environmental change. Quat. Sci. Rev. 28, 449–468.

Fohlmeister, J., Arps, J., Spotl, C., Schroderritzrau, A., Plessen, B., Gunter, C., Trussel, M., 2018. Carbon and Oxygen isotope fractionation in the water-calcite-aragonite system. Geochem. Cosmochim. Acta 127–139.

Francus P, L.H., Nakagawa, T., Marshall, M., Brown, E., 2009. The potential of high-resolution X-ray fluorescence core scanning: applications in paleolimnology. PAGES News 17, 93–95.

Griffiths, M.L., Drysdale, R.N., Gagan, M.K., Frisia, S., Zhao, J.X., Ayliffe, L.K., et al., 2010. Evidence for Holocene changes in Australian–Indonesian monsoon rainfall from stalagmite trace element and stable isotope ratios. Earth Planet Sci. Lett. 292 (1), 27–38.

Guo, C.Q., Zhou, X., Pan, L.Y., 2015. Analysis of drought and flood disasters in karst area of southwest China from 1900 to 2012. Journal of Water Resources and Water Engineering 26, 12–15 (in Chinese with English abstract).

Han, L.-Y., Li, T.-Y., Cheng, H., Edwards, R.-L., Shen, C.-C., Li, H.-C., Zhang, T.-T., 2016. Potential influence of temperature changes in the Southern Hemisphere on the evolution of the Asian summer monsoon during the last glacial period. Quat. Int. 392, 239–250.

Hartland, A., Fairchild, I.J., Lead, J.R., Borsato, A., Baker, A., Frisia, S., et al., 2012. From soil to cave: transport of trace metals by natural organic matter in karst dripwaters. Chem. Geol. 304, 68–82.

Hartland, A., Fairchild, I.J., Lead, J.R., Zhang, H., Baalousha, M., 2011. Size, speciation and lability of nom–metal complexes in hyperalkaline cave dripwater. Geochem. Cosmochim. Acta 75 (23), 7533–7551.

Haug, G.H., Hughen, K.A., Sigman, D.M., Peterson, L.C., Röhl, U., 2001. Southward migration of the intertropical convergence zone through the Holocene. Science 293, 1304–1308.

Hercman, H., Pawlak, J., 2012. MOD-AGE: an age-depth model construction algorithm. Quat. Geochronol. 12, 1–10.

Hu, C., Henderson, G.M., Huang, J., Xie, S., Sun, Y., Johnson, K.R., 2008. Quantification of Holocene Asian monsoon rainfall from spatially separated cave records. Earth Planet Sci. Lett. 266 (3), 221–232.

Hu, C.Y., Huang, J.H., Fang, N.Q., Xie, S.C., Henderson, G.M., Cai, Y.J., 2005. Adsorbed silica in stalagmite carbonate and its relationship to past rainfall. Geochem. Cosmochim. Acta 69, 2285–2292.

Jaffey, A.H., Flynn, K.F., Glendenin, L.E., Bentley, W.C., Essling, A.M., 1971. Precision measurement of half-lives and specific activities of ^{235}U and ^{238}U. Phys. Rev. C 4, 1889–1906.

Johnson, K.R., Hu, C.Y., Belshaw, N.S., Henderson, G.M., 2006. Seasonal trace-element and stable-isotope variations in a Chinese speleothem: the potential for high-resolution paleomonsoon reconstruction. Earth Planet Sci. Lett. 244, 394–407.

Karmann, I., Cruz, F.W., Viana, O., Burns, S.J., 2007. Climate influence on geochemistry parameters of waters from Santana-Perolas cave system, Brazil. Chem. Geol. 244, 232–247.

Kathayat, G., Cheng, H., Sinha, A., Yi, L., Li, X., Zhang, H., Li, H., Ning, Y., Edwards, R.L., 2017. The Indian monsoon variability and civilization changes in the Indian subcontinent. Science Advances 3.

Kathayat, G., Cheng, H., Sinha, A., Yi, L., Li, X., Zhang, H., Li, H., Ning, Y., Edwards, R.L., 2017. The Indian monsoon variability and civilization changes in the Indian subcontinent. Sci. Adv. 3.

Kim, S.T., O'Neil, J.R., Hillaire-Marcel, C., Mucci, A., 2007. Oxygen isotope fractionation between synthetic aragonite and water: influence of temperature and Mg^{2+} concentration. Geochem. Cosmochim. Acta 71 (19), 4704–4715.

Li, D., Tan, L., Guo, F., Cai, Y., Sun, Y., Xue, G., Gao, Y., 2019. Application of Avaatech X-ray fluorescence core-scanning in Sr/Ca analysis of speleothems. Sci. China Earth Sci. 62 (6), 964–973.

Li, J.P., Zeng, Q.C., 2003. A new monsoon index and the geographical distribution of the global monsoons. Adv. Atmos. Sci. 20 (2), 299–302.

Li, J.-Y., Li, T.-Y., 2018. Seasonal and annual changes in soil/cave air pCO$_2$ and the δ^{13}C DIC of cave drip water in response to changes in temperature and rainfall. Appl. Geochem. 93, 984-101.

Lechleitner, F.A., Breitenbach, S.F.M., Rehfeld, K., Ridley, H.E., Asmerom, Y., Prufer, K.M., et al., 2017. Tropical rainfall over the last two millennia: evidence for a low-latitude hydrologic seesaw. Sci. Rep. 7.

Li, T.-Y., C, H., Tian, Lijun, Suarez, Marina B., Gao, Yongli, 2018. Variation of δ^{13}C in plant-soil-cave systems in karst regions with different degrees of rocky desertification in southwest China. J. Cave Karst Stud. 80, 212–228.

Li, T.-Y., Li, H., Xiang, X., Kuo, T.-S., Li, J., Zhou, F., Chen, H., Peng, L., 2012. Transportation characteristics of δ^{13}C in the plants-soil-bedrock-cave system in Chongqing karst area. Sci. China Earth Sci. 55, 685–694.

Li, T.-Y., Shen, C.-C., Li, H.-C., Li, J.-Y., Chang, H.-W., Song, S.-R., Yuan, D.-X., Lin, C.D.-J., Gao, P., Zhou, L.-P., Wang, J.-L., Ye, M.-Y., Tang, L.-L., Xie, S.-Y., 2011. Oxygen and carbon isotopic systematics of aragonite speleothems and water in Furong Cave, Chongqing, China. Geochem. Cosmochim. Acta 75, 4140–4156.

Liu, D.B.W.Y., Cheng, H., Edwards Lawrence, R., Kong, X.G., Li, T.Y., 2016. Strong coupling of centennial-scale changes of Asian monsoon and soil processes

derived from stalagmite $\delta^{18}O$ and $\delta^{13}C$ records, Southern China. Quat. Res. 85, 333–346.

Liu, Z.Q., H, L., Xiong, K.N., Yuan, D.X., Ying, B., Xu, X.M., Li, J.Y., 2008. Implication for sampling paleo-climate indicators by monitoring seasonal variations of δD and $\delta^{18}O$ in cave waters. Carsol. Sin./Zhong Guo Yan Rong 27, 139–144.

Liu, Y.H., Henderson, G.M., Hu, C.Y., Mason, A.J., Charnley, N., Johnson, K.R., Xie, S.C., 2013. Links between The east asian monsoon and North Atlantic climate during the 8200 year event. Nat. Geosci. 6 (2), 117.

Liu, Z., Sun, H., Li, H., Wan, N., 2011. $\delta^{13}C$, $\delta^{18}O$ and deposition rate of tufa in Xiang Shui river, SW China: implications for land-cover change caused by climate and human impact during the late Holocene. Geological Society London Special Publications 352 (1), 85–96.

Maher, B.A., Thompson, R., 2012. Oxygen isotopes from Chinese caves: records not of monsoon rainfall but of circulation regime. J. Quat. Sci. 27, 615–624.

McDermott, F., 2004. Palaeo-climate reconstruction from stable isotope variations in speleothems: a review. Quat. Sci. Rev. 23, 901–918.

Mcmillan, E.A., Fairchild, I.J., Frisia, S., Borsato, A., Mcdermott, F., 2005. Annual trace element cycles in calcite–aragonite speleothems: evidence of drought in the western Mediterranean 1200–1100 yr BP. J. Quat. Sci. 20 (5).

Moy, C.M., Seltzer, G.O., Rodbell, D.T., Anderson, D.M., 2002. Variability of El Niño/ Southern oscillation activity at millennial timescales during the Holocene epoch. Nature 420 (6912), 162–165.

Oster, J.L., Montanez, I.P., Kelley, N.P., 2012. Response of a modern cave system to large seasonal precipitation variability. Geochem. Cosmochim. Acta 91, 92–108.

Pausata, F.S.R., Battisti, D.S., Nisancioglu, K.H., Bitz, C.M., 2011. Chinese stalagmite $\delta^{18}O$ controlled by changes in the Indian monsoon during a simulated Heinrich event. Nat. Geosci. 4, 474–480.

Reeder, R.J., Nugent, M., Lamble, G.M., Tait, C.D., Morris, D.E., 2000. Uranyl incorporation into calcite and aragonite: XAFS and luminescence studies. Environ. Sci. Technol. 34 (4), 638–644.

Rein, B., Lückge, A., Reinhardt, L., Sirocko, F., Wolf, A., Dullo, W.C., 2005. El Niño variability off Peru during the last 20,000 years. Paleoceanography 20 (4).

Richter, D.K., Gotte, T., Niggemann, S., Wurth, G., 2004. Ree^{3+} and Mn^{2+} activated cathodoluminescence in late glacial and Holocene stalagmites of central Europe: evidence for climatic processes? Holocene 14 (5), 759–768.

Riechelmann, S., Schroderritzrau, A., Wassenburg, J.A., Schreuer, J., Richter, D.K., Riechelmann, D.F., Immenhauser, A., 2014. Physicochemical characteristics of drip waters: influence on mineralogy and crystal morphology of recent cave carbonate precipitates. Geochem. Cosmochim. Acta 13–29.

Rossi, C., Lozano, R.P., 2016. Hydrochemical controls on aragonite versus calcite precipitation in cave dripwaters. Geochem. Cosmochim. Acta 70–96.

Schneider, T., Bischoff, T., Haug, G.H., 2014. Migrations and dynamics of the intertropical convergence zone. Nature 513 (7516), 45–53.

Schwertmann, U., 1971. Transformation of hematite to goethite in soils. Nature 232 (5313), 624–625.

Scroxton, N., Burns, S.J., McGee, D., Hardt, B., Godfrey, L.R., Ranivoharimanana, L., Faina, P., 2017. Hemispherically in-phase precipitation variability over the last 1700 years in a Madagascar speleothem record. Quat. Sci. Rev. 164, 25–36.

Shen, C.-C., Wu, C.-C., Cheng, H., Edwards, R.-L., Hsieh, Y.-T., Gallet, S., Hori, M., 2012. High-precision and high-resolution carbonate ^{230}Th dating by MC-ICP-MS with SEM protocols. Geochem. Cosmochim. Acta 99, 71–86.

Song, M.Y., Kwon, S.N., Park, Hye Ryoung, 2013. Characterization of a magnesium-based alloy after hydriding-dehydriding cycling (n=1–150). Met. Mater. Int. 19 (5), 1139–1144.

Tan, L.C., Cai, Y.J., An, Z.S., Cheng, H., Shen, C.C., Breitenbach, S.F., Du, Y., 2015. A Chinese cave links climate change, social impacts, and human adaptation over the last 500 years. Sci. Rep. 5, 12284.

Tan, L.C., Cai, Y.J., Cheng, H., Edwards, L.R., Lan, J., Zhang, H., Li, D., Ma, L., Zhao, P., Gao, Y., 2018. High resolution monsoon precipitation changes on southeastern Tibetan Plateau over the past 2300 years. Quat. Sci. Rev. 195, 122–132.

Tan, L.C., Shen, C.C., Löwemark, L., Chawchai, S., Edwards, R.L., Cai, Y., Partin, J.W., 2019. Rainfall variations in central Indo-Pacific over the past 2,700 y. Proc. Natl. Acad. Sci. Unit. States Am. 116 (35), 17201–17206.

Tan, M., 2016. Circulation background of climate patterns in the past millennium: uncertainty analysis and re-reconstruction of ENSO-like state. Sci. China Earth Sci. 59 (6), 1225–1241.

Tan, M., 2014. Circulation effect: response of precipitation $\delta^{18}O$ to the ENSO cycle in monsoon regions of China. Clim. Dynam. 42, 1067–1077.

Tarutani, T., Clayton, R.N., Mayeda, T.K., 1969. The effect of polymorphism and magnesium substitution on oxygen isotope fractionation between calcium carbonate and water. Geochem. Cosmochim. Acta 33, 987–996.

Toth, L.T., Aronson, R.B., Vollmer, S.V., Hobbs, J.W., Urrego, D.H., Cheng, H., et al., 2012. ENSO drove 2500-year collapse of eastern Pacific coral reefs. Science 337 (6090), 81–84.

Vansteenberge, S., Winter, N.J.D., Sinnesael, M., Xueqin, Z.X.Z., Claeys, P., 2019.

Benchtop μXRF as a tool for speleothem trace elemental analysis: validation, limitations and application on an eemian to early weichselian (125–97 ka) stalagmite from Belgium. Palaeogeogr. Palaeocl. 538, 109460.

Wang, P.X., Wang, B., Cheng, H., Fasullo, J., Guo, Z., Kiefer, T., Liu, Z., 2017. The global monsoon across time scales: mechanisms and outstanding issues. Earth Sci. Rev. 174, 84–121.

Wan, N.-J., Li, H.-C., Liu, Z.Q., Yang, H.Y., Yuan, D.Y., Chen, Y.H., 2011. Spatial variations of monsoonal rain in eastern China: instrumental, historic and speleothem records. J. Asian Earth Sci. 40, 1139–1150.

Wang, Y.J., Cheng, H., Edwards, R.L., He, Y., Kong, X., An, Z., Wu, J., Kelly, M.J., Dykoski, C.A., Li, X., 2005. The Holocene Asian monsoon: links to solar changes and North Atlantic climate. Science 308, 854–857.

Wassenburg, J.A., Immenhauser, A., Richter, D.K., Jochum, K.P., Fietzke, J., Deininger, M., Goos, M., Scholz, D., Sabaoui, A., 2012. Climate and cave control on Pleistocene/Holocene calcite-to-aragonite transitions in speleothems from Morocco: elemental and isotopic evidence. Geochem. Cosmochim. Acta 92, 23–47.

Wassenburg, J.A., Riechelmann, S., Schroderritzrau, A., Riechelmann, D.F., Richter, D.K., Immenhauser, A., Scholz, D., 2020. Calcite Mg and Sr partition coefficients in cave environments: implications for interpreting prior calcite precipitation in speleothems. Geochem. Cosmochim. Acta 581–596.

Wassenburg, J.A., Scholz, D., Jochum, K.P., Cheng, H., Oster, J.L., Immenhauser, A., Breitenbach, S.F., 2016. Determination of aragonite trace element distribution coefficients from speleothem calcite–aragonite transitions. Geochem. Cosmochim. Acta 347–367.

Wong, C.I., Banner, J.L., Musgrove, M., 2011. Seasonal dripwater Mg/Ca and Sr/Ca variations driven by cave ventilation: implications for and modeling of speleothem paleoclimate records. Geochem. Cosmochim. Acta 75, 3514–3529.

Wu, Z.H., Huang, N.E., 2009. Ensemble empirical mode decomposition: a noise-assisted data analysis method. Adv. Adapt. Data Anal. 1–41.

Xiao, X., Haberle, S.G., Shen, J., Yang, X., Han, Y., Zhang, E., Wang, S., 2014. Latest Pleistocene and Holocene vegetation and climate history inferred from an alpine lacustrine record, northwestern Yunnan Province, southwestern China. Quat. Sci. Rev. 86, 35–48.

Yang, X.Q., Chen, X.M., Li, Zhou, L.C., Chen, L., Nan, J.K., et al., 2011. Study on composition and content variation of clay mineral of soil under different stages of rock desertification in karst region, southwest China. J. Earth Sci. Environment 33 (4), 417–420 (In Chinese).

Yang, S.H., Chen, S.T., Wang, Y.J., Zhang, Z.Q., Zeng, Y.L., 2017. Comparison of oxygen-carbon isotopes from a Holocene stalagmite by EEMD method. Geogr. Res. 36, 8.

Yang, Y., Yang, R., Cao, J., Zhao, J., Cheng, H., Wang, J., 2019. Relationship between the Asian summer monsoon circulation and speleothem $\delta^{18}O$ of Xiaobailong cave. Clim. Dynam. 1–12.

Yuan, D.X., 2015. Scientific innovation in karst resources and environment research field of China. Carsol. Sin./Zhong Guo Yan Rong 34, 98–100 (in Chinese with English abstract).

Zeng, S., Jiang, Y., Liu, Z., 2016. Assessment of climate impacts on the karst-related carbon sink in SW China using MPD and GIS. Global Planet. Change 144, 171–181.

Zhang, H., Cai, Y., Tan, L., Qin, S., An, Z., 2014a. Stable isotope composition alteration produced by the aragonite-to-calcite transformation in speleothems and implications for paleoclimate reconstructions. Sediment. Geol. 309, 1–14.

Zhang, P., Cheng, H., Edwards, R., Chen, F., Wang, Y., Yang, X., et al., 2008. A test of climate, sun, and culture relationships from an 1810-year Chinese cave record. Science 322 (5903), 940–942.

Zhang, H., Griffiths, M.L., Chiang, J.C.H., Kong, W., Wu, S., Atwood, A., Huang, J., Cheng, H., Ning, Y., Xie, S., 2018. East Asian hydroclimate modulated by the position of the westerlies during Termination I. Science 362.

Zhang, Z., Leduc, G., Sachs, J.P., 2014b. El Niño evolution during the Holocene revealed by a biomarker rain gauge in the Galápagos Islands. Earth Planet Sci. Lett. 404, 420–434.

Zhao, K., Wang, Y., Edwards, R.L., Cheng, H., Kong, X., Liu, D., Yang, X., 2020. Late Holocene monsoon precipitation changes in southern China and their linkage to Northern Hemisphere temperature. Quat. Sci. Rev. 232, 106191.

Zhao, K., Wang, Y., Edwards, R.L., Cheng, H., Liu, D., Kong, X., Ning, Y., 2016. Contribution of ENSO variability to the East Asian summer monsoon in the late Holocene. Palaeogeogr. Palaeoclimatol. Palaeoecol. 449, 510–519.

Zhou, H., Chi, B., Michael, L., Zhao, J., Yan, J., Alan, G., et al., 2008. High-resolution and precisely dated record of weathering and hydrological dynamics recorded by manganese and rare-earth elements in a stalagmite from central China. Quat. Res. 69 (3), 438–446.

Zhu, Z., Feinberg, J.M., Xie, S., Bourne, M.D., Huang, C., Hu, C., Cheng, H., 2017. Holocene ENSO-related cyclic storms recorded by magnetic minerals in speleothems of central China. Proc. Natl. Acad. Sci. U.S.A. 114, 852–857.